New examination of the Raman lidar technique for water vapor and aerosols I: evaluating the temperature dependent lidar equations – Popular Summary

Submitted to Applied Optics

David N. Whiteman

A Raman Lidar is an active remote sensing system that uses a laser to excite elastic and ineslatic scattering in atmospheric particles and molecules and senses the backscattered radiation using a telescope, optical detectors and electronics. In the last few years, the use of Raman lidar for providing high spatial and temporal resolution measurements of water vapor and aerosols has greatly expanded in various locations around the world. This increase in the number or Raman lidar systems is particularly apparent in Europe where the European Aerosol Lidar Network (EARLINET) has recently been established. However, a consistent, modern treatment of the analytical techniques required to derive meteorological quantities from these lidar measurements does not exist. This paper is the first of a two-paper sequence providing just such a treatment. This paper provides detailed information on how to evaluate the lidar equations for both elastic and inelastic scattering including the effects of the temperature sensitivity of Raman scattering. For the first time, numerical simulations of the complete Raman spectrum of water vapor are used in this evaluation. Other details considered in this treatment include accurate calculations of Rayleigh scattering, the influence of temperature dependence on aerosol extinction, correction for photon pulse pile up in detectors and the influence of multiple scattering on extinction measurements.

New examination of the Raman lidar technique for water vapor and aerosols I: evaluating the temperature dependent lidar equations

David N. Whiteman
NASA/Goddard Space Flight Center
Greenbelt, MD 20771

Abstract

The intent of this paper and its companion is to compile together the essential information required for the analysis of Raman lidar water vapor and aerosol data acquired using a single laser wavelength. In this first paper several details concerning the evaluation of the lidar equation when measuring Raman scattering are considered. These details include the influence of the temperature dependence of both pure rotational and vibrational-rotational Raman scattering on the lidar profile. These are evaluated for the first time using a new form of the lidar equation. The results indicate that, for the range of temperatures encountered in the troposphere, the magnitude of the temperature dependent effect can reach 10% or more for narrowband Raman water vapor measurements. Also the calculation of atmospheric transmission is examined carefully including the effects of depolarization. Different formulations of Rayleigh cross section determination commonly used in the lidar field are compared revealing differences up to 5% among the formulations. The influence of multiple scattering on the measurement of aerosol extinction using the Raman lidar technique is considered as are several photon pulse-pileup correction techniques. OCIS # 010.3640, 010.3920, 999.9999

1 Introduction

The Raman lidar is well established today as a leading research tool in the study of numerous areas of importance in the atmospheric sciences. The Raman lidar has been used to study the passage of frontal systems [1], stratospheric aerosols due to volcanic eruptions [2], atmospheric temperature variations in cirrus clouds [3], long term variation of water vapor and aerosols at a mid-continental site [4], cloud liquid water [5], cirrus cloud optical [6] and physical [7] properties, the influence of thin cirrus clouds on satellite retrievals of water vapor [8], hygroscopic growth of aerosols [9], cloud base height detection [10], multi-wavelength Raman lidar measurements of aerosols enabling remote characterization of aerosols [11] [12] and other topics. Recently, numerical simulation has been used to demonstrate that an airborne Raman water vapor lidar offers a dramatic increase in temporal and spatial resolution compared to existing differential absorption lidars under nighttime conditions [13]. Of all these uses of Raman lidar, perhaps the most common has been for the measurement of water vapor and aerosols using either a UV or visible radiation source. Yet, despite the availability of several good references describing these measurements of water vapor and aerosols [14] [15] [1] [16] [17] [18] [9] [19] [4] [20], the essential material needed for analyzing these Raman lidar data has not been compiled together previously. With several new Raman lidars being developed in Europe as a part of the European Aerosol Lidar Network (EARLINET) [21] [22] and other activities, it seemed an appropriate time to create such a reference. Furthermore, and perhaps more importantly, recent work in numerical simulation of the Raman water vapor spectrum now permits the temperature sensitivity of Raman scattering from water vapor to be evaluated as has been possible for the rotational Raman scattering from diatomic molecules [23] [24] [25] since the early days of lidar [26] and before [27].

This first paper in a two-paper sequence considers the details of evaluating the lidar equation including the temperature sensitivity of Raman scattering. The companion paper [28] (to be referred to as part II) will then consider forming the ratios of lidar signals for the study of water vapor and aerosols. The general organization of this paper is as follows. First, as reference material, the traditional lidar equations are presented. Simulations of the temperature sensitivity of the Raman water vapor spectrum are then presented offering motivation for the development of a new form of the temperature dependent lidar equations. The temperature dependence is then formulated in a new way that permits its influence to be confined to a single term that becomes a multiplier of the traditional lidar equations. A detailed description of the calculation of atmospheric transmission including extinction both due to molecules and aerosols is then presented where the effects of temperature sensitivity are propagated through aerosol extinction equations. Other effects that must be accounted for in the evaluation of the lidar equation are multiple scattering and photon pulse pileup. These are considered in appendices.

2 Traditional single scattering Rayleigh-Mie and Raman lidar equations

Equations will now be presented for Rayleigh-Mie and Raman Lidars. In order to avoid confusion, a few definitions will first be given. The term "Rayleigh scattering" will be used to signify the combination of Cabannes and rotational Raman scattering [29] [30]. This recognizes the fact [29] [30] that what Lord Rayleigh [31] [32] actually detected was a combination of elastic and rotational Raman scattering. The term "Mie" scattering will be used to refer to scattering by particles of any shape even though the Mie theory [33] only pertains to spherical particles. The term "Rayleigh-Mie" lidar will then be used here to refer to systems that measure elastically scattered light from both molecules and particles of any shape as well as inelastically scattered pure rotational Raman scattering. Finally, while changes in transmission versus wavelength are due mostly to the characteristics of the interference filter or monochromator used in a particular lidar channel, other optics in the system can also display wavelength dependent transmission efficiency. Therefore, the term "passband" will be used to describe the transmission function of a particular lidar optical channel.

Now the background-subtracted power received by a detector as a function of range in a Rayleigh-Mie lidar system, assuming no multiple scattering and that the received signal is at a single discrete wavelength, can be expressed as

$$P\left(\lambda_L,r\right)=\frac{O\left(r\right)P_0\left(\lambda_L\right)A\xi\left(\lambda_L\right)\left(N_R\left(r\right)\frac{d\sigma_R\left(\lambda_L,\pi\right)}{d\Omega}+\beta_\pi^{aer}\left(\lambda_L,r\right)\right)}{r^2}\exp\left(-2\int_0^r\alpha(\lambda_L,r^{'})dr^{'}\right) \tag{1}$$

$P\left(\lambda_L,r\right)$ is the backscattered power (after subtracting any background contribution due, for example, to skylight or detector noise) received at the laser wavelength, λ_L, as a function of range, r. $O_R\left(r\right)$ is the Rayleigh-Mie channel overlap function, $P_0\left(\lambda_L\right)$ is the output power of the laser at the laser wavelength, λ_L. $N_R\left(r\right)$ is the number density of "air" molecules and $d\sigma_R\left(\lambda_L,\pi\right)/d\Omega$ is the Rayleigh backscatter cross section at the laser wavelength. $\beta_\pi^{aer}\left(\lambda_L,r\right)$ is the backscatter coefficient at the laser wavelength and at range r due to Mie scattering. $\xi\left(\lambda_L\right)$ is the total lidar receiver optical efficiency at the laser wavelength and includes factors such as the reflectivity of the telescope, the transmission of conditioning optics, the transmission of any filters and the quantum efficiency of the detector. A is the receiver telescope area. The exponential factor gives the two-way atmospheric transmission, where $\alpha(\lambda_L,r)$ is the total extinction coefficient at the laser wavelength due to scattering and absorption by molecules, particles and any other atmospheric constituents such as water droplets or ice crystals as a function of range along the path of the laser beam.

The corresponding single scattering Raman lidar equation for a vibrationally-scattered Raman species X, in its traditional form, is given in equation 2

$$P\left(\lambda_X,r\right) = \frac{O_X\left(r\right)\ P_0\left(\lambda_L\right)\ N_X\left(r\right)\ \frac{d\sigma_X\left(\lambda_L,\pi\right)}{d\Omega}A\ \xi\left(\lambda_X\right)}{r^2}\exp\left(-\int_0^r\{\alpha(\lambda_L,r^{'})+\alpha(\lambda_X,r^{'})\}dr^{'}\right) \tag{2}$$

where now it should be noted that the atmospheric transmission function includes a term at the laser wavelength, λ_L, for the transmission along the output path and another for the backscattered signal at the wavelength, λ_X, which has been shifted from the laser wavelength due to inelastic Raman scattering by molecular species X. $N_X\left(r\right)$ is the number density of molecular species X that is being excited and $d\sigma_X\left(\lambda_L,\pi\right)/d\Omega$ is the pertinent Raman backscatter cross section.

3 Temperature dependence of the lidar equations

As stated, equations 1 and 2 assume that the return signal can be considered to be at a discrete wavelength. In the case of the Raman signals excited in the visible or near UV by lasers such as the frequency doubled (532.07 nm) or tripled Nd:YAG (354.71 nm), the desired signal actually covers an interval that can range from a few tenths of nanometers (e. g. the OH-stretch region of water vapor) to a few nanometers (rotational-vibrational spectrum from diatomic molecules such as N_2 and O_2). In the case of the Rayleigh-Mie signal at this wavelength, there is pure rotational Raman scattering from nitrogen, oxygen and other molecules that is centered on the laser wavelength and that covers a band of a few nanometers as well [34].

Therefore, there is Raman scattering to be considered in both the Rayleigh-Mie and Raman signals. The individual line strengths in a Raman spectrum are temperature dependent. In general, this temperature dependence should be considered when formulating either the Rayleigh-Mie or Raman lidar equations since, if the passband used to make the measurements transmits any Raman signals, the intensity of the backscattered signal per molecule may be temperature sensitive. This effect has been carefully considered before by Sherlock et. al. [35] who developed temperature dependent Raman lidar equations for the water vapor mixing ratio calculations. These earlier efforts accounted for the effects of temperature sensitivity in the absolute calibration of a water vapor Raman lidar. However, their Raman scattering model did not include the anisotropic part of the water vapor spectrum, which can now be included due to theoretical work that has occured recently [36]. The current ability to simulate the OH-stretch portion of the Raman water vapor spectrum including the isotropic and anisotropic components eliminates one of the largest error sources present in the absolute calibration of a Raman water vapor lidar that was pursued by Sherlock et. al. [35]. New forms of the lidar equations will be derived that permit the temperature effect to be easily propagated through subsequent derivations.

To illustrate the effect of the temperature dependence of Raman scattering, consider the case of the Raman vibrational signals. The molecules are essentially all in their ground state at atmospheric temperatures as determined by the Maxwell-Boltzmann distribution. A vibrational Raman scattering event is therefore overwhelmingly likely to involve a transition from the ground state to the Stokes (higher energy) part of the spectrum. Thus, at atmospheric temperatures, the integral across the entire Raman Stokes band will be temperature insensitive (the transition will appear *somewhere* in the spectrum). However, if only a portion of the band is transmitted, there will in general be a temperature dependence to the transmitted intensity [37], although there are some exceptions to this that will be discussed later. For the case of pure rotational Raman scattering, however, the rotational states differ little in energy from the ground state so that there is a significant probability that some of the rotational states will be excited at atmospheric temperatures. (Considering the N_2 molecule, the $J = 0$ state for pure rotational Raman scattering is approximately 10^5 times more likely to be excited at $T = 290K$ than is the first vibrational transition.) Thus, the integral of neither the O nor the S branch of the rotational Raman spectrum is, by itself, temperature independent however the sum of the two is.

If the lidar system efficiency is constant over the wavelength interval containing a complete Raman feature, either vibrational or pure rotational, then there is no temperature sensitivity to the received signals [37]. Also, there can be narrow portions of certain Raman spectra that are temperature independent. This exists for example at the isosbestic point of liquid water (~3425 cm^{-1}) [38] as well as in the spectral vicinity of $J = 7, 8$ for the pure rotational spectra of N_2 and O_2 [39]. However, in general, if narrow filters are used in the detection of Raman features, the total lidar system efficiency is likely to change as a function of temperature as the strengths of the individual lines in the Raman spectrum change [35] imparting a temperature sensitivity to the measurement.

This temperature sensitivity can be useful for atmospheric measurements. The intensities of rotational and vibrational-rotational lines from N_2 and O_2 are well predicted by diatomic molecule line strength models [27] [23]. These models have been used to enable atmospheric temperature measurements using Raman lidar [26] [40] [3]. These models will be used here to evaluate the temperature sensitivity of the Raman pure rotational and vibrational-rotational N_2 and O_2 signals for different passband widths and center positions.

3.1 Raman water vapor simulations

Water is an asymmetric top molecule that possesses a much more complicated spectrum than does either N_2 or O_2. The numerical simulation of the spectrum from asymmetric top molecules such as water vapor has, in the past, been available to a very limited number of researchers [41] [42] [43] [44]. However, a recent publication by Avila et. al. [36] now makes it possible to easily simulate the Raman OH-stretch spectrum for water vapor over a range of temperatures. These results permit the anisotropic component of the Raman water vapor spectrum to be included thus permitting the full temperature sensitivity of a Raman water vapor lidar system to be evaluated for the first time.

This new modeling capability has been used to simulate spectra of the Raman OH-stretch region of water vapor at two different temperatures. They are shown in figure 1. These spectra have been simulated using 0.5 cm^{-1} resolution at $200K$ and $295K$. As temperature increases, the quantum number transitions that are farther from the band origin of 3657 cm^{-1} (i.e. higher J number) become increasingly more likely to be excited. This implies that for a lidar system characterized by a narrow passband, simulated in the figure using a Gaussian transmission function of ~18 cm^{-1} width (corresponding to ~0.3 nm at ~407.5 nm, the location of the water vapor ν_1 transition when excited by the tripled Nd:YAG laser - 354.7 nm) and shown with a dash-dot line, the integrated intensity of the Raman feature across the passband shown will be temperature sensitive. It should be mentioned that the atmospheric feature that is typically measured by a Raman water vapor lidar is often referred to as the ν_1 band of water vapor. However, at atmospheric temperatures, this portion of the spectrum also includes contributions from ν_3, which must be considered for accurate simulations of the spectra [36]. Contributions from ν_2 or its overtones are not significant below temperatures of 400 K [45] [46].

The Raman water vapor differential backscatter cross section was determined for temperatures between 200 K and 300 K in order to evaluate the temperature sensitivity of the signal transmitted by the passband shown in figure 1. The integral of the passband centered at 3654 cm^{-1} shown in figure 1 and the Raman spectrum was performed at each of the temperatures. The results are plotted in figure 2. For these calculations, the area under the passband was normalized to unity. The results shown in figure 2 indicate that there is approximately a 7% change in transmitted intensity between $200K$ and $300K$. This implies that there would be an increase in the sensitivity of a narrowband water vapor lidar in the upper troposphere, where atmospheric temperatures are colder, compared to low altitudes.

These results suggest a reformulation of equations 1 and 2 in a manner that makes this temperature dependence more explicit. One reformulation has been published previously [35]. In the next section, a new formulation will be presented that permits all the temperature sensitivity of the equation to reside in a single term by which the traditional lidar equations can be multiplied.

4 Temperature dependent lidar equations

4.1 Rayleigh-Mie lidar equation

The background-subtracted Rayleigh-Mie lidar equation, analogous to equation 1, but containing the temperature dependence of rotational Raman scattering explicitly, is given below

$$\begin{aligned} P\left(\Delta\lambda_R, r\right) &= \frac{O_R\left(r\right)P_0\left(\lambda_L\right)A\left(\int_{\Delta\lambda_R}\frac{N_R(r)d\sigma_R\left(\lambda^{'},\pi,T\right)}{d\Omega}\xi\left(\lambda^{'}\right)d\lambda^{'}+\beta_{\pi}^{aer}\left(\lambda_L,r\right)\xi\left(\lambda_L\right)\right)}{r^2} \\ &\quad \times\exp\left(-2\int_0^r\alpha(\lambda_L,r^{'})dr^{'}\right) \end{aligned} \tag{3}$$

$P\left(\Delta\lambda_R, r\right)$ is the background-subtracted, received power for the passband $\Delta\lambda_R$, which contains the combined Rayleigh (Cabannes and rotational Raman) and Mie signals, as a function of range. This is the single scattering lidar equation in a form which accounts for the possibility that the lidar system optical efficiency, $\xi\left(\lambda^{'}\right)$, may change over the range of wavelengths $\Delta\lambda_R$, the wavelength range over which there is significant tranmission by the lidar system. The subscript R is used to refer to the Rayleigh-Mie signal. It should be noted here that the laser bandwidth is implicitly assumed to be negligibly small. This is a good approximation when using Nd:YAG lasers with bandwidth ~1 cm^{-1} since narrowband interference filters that are used in Raman lidar studes are more than an order of magnitude wider than this. But XeF excimer lasers, for example, are known to possess an output spectrum covering ~2 nm around its nominal emission wavelength of 351.1 nm [37]. In such a case an integral over the wavelengths covered by the laser output spectrum would be required in equation 1 for completeness.

The Rayleigh signal consists of a narrow elastically scattered signal at the laser wavelength (Cabannes scattering) along with inelastic (frequency-shifted) pure rotational lines, due primarily to N_2 and O_2, on both sides of the

Cabannes feature. For practical purposes, the rotational spectrum may be described by quantum numbers up to approximately 30 [47], which corresponds to a wavelength range of a few nanometers when excited in the UV or visible region. In order to measure this spectrum, a range of wavelengths $\Delta\lambda_R$ is sampled by the lidar system. It is possible that the lidar system transmission efficiency will change over this wavelength range. The notation $d\sigma_R\left(\lambda^{'},\pi,T\right)/d\Omega$, which includes the explicit wavelength temperature dependences, is thus used for the differential backscatter cross section for the combined effects of Rayleigh and pure rotational Raman scattering. This formulation allows the influence of the changing intensity of the rotational Raman lines as a function of wavelength and temperature to be quantified. These changes can introduce a temperature sensitivity to the measured Rayleigh signal. Calculations of the rotational Raman line intensities of these diatomic molecules as a function of temperature [27] [23] coupled with knowledge of the lidar system transmission characteristics are needed to evaluate the temperature dependence of equation 3. Pure rotational scattering from other molecules such as carbon dioxide and water vapor [48] also exist but at such small levels as to be insignificant for the present purposes.

Aerosols in the atmosphere are much heavier than molecules. The Doppler broadening of the Mie signal due to aerosols will therefore be much less than that for molecules. Because of this, the Mie signal from aerosols has a narrower spectral width than the elastic scattering from molecules. Thus, for the passband widths considered here, the single wavelength notations used in the traditional lidar equation for $\beta_\pi^{aer}(\lambda_L,r)$, the aerosol backscatter coefficient, and $\xi(\lambda_L)$,the total receiver system efficiency at the laser wavelength, are still appropriate in the temperature dependent form of the equation.

4.2 Raman lidar equation

The temperature dependent equation for the signal from a vibrationally-excited Raman species X is

$$\begin{aligned} P(\Delta\lambda_X,r) &= \frac{O_X(r)\ P_0(\lambda_L)\ N_X(r)\ A\ \int_{\Delta\lambda_X}\frac{d\sigma_X\left(\lambda^{'},\pi,T\right)}{d\Omega}\,\xi\left(\lambda^{'}\right)\,d\lambda^{'}}{r^2} \\ &\quad\times\exp\left(-\int_0^r\{\alpha(\lambda_L,r^{'})+\alpha\lambda_X,r^{'}()\}dr^{'}\right) \end{aligned} \tag{4}$$

where now $\Delta\lambda_X$ refers to the passband over which the Raman vibrational signal is detected. Notice here the lack of the aerosol backscatter term $\beta_{\pi}^{aer}(\lambda_L, r)\,\xi(\lambda_L)$ since only inelastically scattered radiation due to molecular interactions is present in this signal. A temperature dependent function will now be introduced that will permit equations 3 and 4 to be expressed in a more straightforward manner. This temperature dependent function simplifies previous formulations [35] and will permit the influence of temperature dependence to be easily propagated through the traditional Raman lidar formulas [28].

4.3 The function $F_X(T)$

Consider the case of the Raman scattered signal from water vapor expressed using equation 4 by replacing X by H. The integral over $\Delta\lambda_H$ may be expressed as

$$\int_{\Delta\lambda_H} \frac{d\sigma_H\left(\lambda', \pi, T\right)}{d\Omega}\,\xi\left(\lambda'\right)\,d\lambda' = F_H(T)\frac{d\sigma_H(\pi)}{d\Omega}\,\xi(\lambda_H) \tag{5}$$

So that $F_H(T)$ becomes

$$F_H(T) = \frac{\int_{\Delta\lambda_H} \frac{d\sigma_H\left(\lambda', \pi, T\right)}{d\Omega}\,\xi\left(\lambda'\right)\,d\lambda'}{\frac{d\sigma_H(\pi)}{d\Omega}\,\xi(\lambda_H)} \tag{6}$$

A new function $F_H(T)$ has been introduced which carries all the temperature dependence of the lidar equation. It contains the effects of any changes in the system transmission efficiency, $\xi(\lambda)$, for wavelengths other than λ_H within the passband $\Delta\lambda_H$. $\xi(\lambda_H)$ is the transmission efficiency at λ_H,where it is assumed that this is the maximum value of the transmission function over the interval $\Delta\lambda_H$. If this is not the case, then the appropriate term here would be $\xi_{\max}(\Delta\lambda_H)$. The notation $d\sigma_H(\pi)/d\Omega$ is used to indicate the total Raman backscatter cross section for water vapor at the stimulating wavelength. For either the tripled Nd:YAG (354.7 nm) or the XeF excimer laser (351 nm) this value is approximately 6.2 $\times 10^{-34}\ m^2 sr^{-1}$ [34] and, at atmospheric temperatures, is essentially constant with temperature. In a typical lidar system, transmission changes that occur within the interval $\Delta\lambda_H$ are determined primarily by the interference filter itself with smaller changes due to other optics such as dichroic beamsplitters. Although the transmission function that describes the passband of a lidar system is due to the characteristics of all optics that intercept the received signal, the interference filter by itself typically determines the majority of the transmission variation within the spectral band of interest. Because of this, in practice it may be more convenient to evaluate $\xi\left(\lambda'\right)$ as a product of interference filter transmission, determined using a spectro-photometer device, and the transmission of the remaining optics determined through the use of, for example, a calibrated lamp source or through atmospheric modeling [35]. The product $F_H(T)\frac{d\sigma_H(\pi)}{d\Omega}$ may be viewed as the effective molecular cross section that is consistent with the use of a monochromatic optical efficiency term, $\xi\left(\lambda_H\right)$, in the lidar equation. This will permit the temperature dependence to be expressed as a simple multiplier of the normal Raman lidar equation. The situation is not so simple in the Rayleigh-Mie lidar equation as will be shown in section 4.5.

Data such as presented in figure 1 may now be used to illustrate the calculation of $F_H(T)$ for the case of a water vapor measurement using the 18 cm^{-1} (0.3 nm at 407.5 nm) full width at half maximum (FWHM) passband also shown in the figure. The function $F_H\left(T\right)$ given in equation 6 may be determined by dividing the values shown in figure 2 by the product the total backscatter cross section $d\sigma_H\left(\pi\right)/d\Omega$ (since figure 2 was generated using a peak lidar system transmission of 1.0). The results in Table 1 indicate that the effective cross section will be between 90% and 96% of the full Raman water vapor OH-stretch cross section over the range of temperatures considered. By contrast, the effective cross section changes by less than 1% when using a 120 cm^{-1} passband for the water vapor measurement. Similar calculations can be done for the Rayleigh (including the pure rotational Raman contribution) and vibrational-rotational Raman signals from diatomic molecules [27] [23] [37]. Those results are also displayed in Table 1 for passband widths in wavenumbers that correspond to 0.3 nm and 2 nm for the various signals excited at 354.7 nm. All passbands are assumed to be centered on their respective spectra. As shown in the table, the percentage change in transmission between 200 K and 300 K for each of these cases is as follows: Rayleigh 24 cm^{-1} filter: 0.09%, Rayleigh 160 cm^{-1} filter: 0.2%, vibrational-rotational O_2 21 (142) cm^{-1} filter: 1.3% (2.4%), vibrational-rotational N_2 20 (134) cm^{-1} filter: 0.4% (1.6%). These calculations illustrate that the temperature dependence of Raman scattering can be a significant effect for vibrational-rotational Raman lidar measurements. For the Rayleigh-Mie lidar, these effects change the results of the non-temperature dependent equation given in 1 by less than 1%. Table 2 can be used to determine the corresponding passbands for doubled Nd:YAG (532.07 nm) excitation. For example, to span 50 $cm^{-1}$of the oxygen feature when excited at 354.7 nm requires a filter of ~0.7 nm whereas spanning the same wavenumber range when excited at 532.07 nm would require a filter width of ~1.7 nm.

Table 1 displays F_X calculated for bandwidths that correspond to 0.3 and 2.0 nm when excited at 354.7 nm where the passband is assumed centered on the spectrum. It is interesting to consider other passband widths for the Rayleigh and three Raman signals. Figure 3 displays the percentage change in F_X, or equivalently transmitted intensity, between 200K and 300K ($I\left(200K\right)/I\left(300K\right) \times 100$) as a function of passband width. The maximum percentage change in transmitted Rayleigh signal is ~0.33% for a passband width of ~95 cm^{-1} (~1.2 nm at 354.7 and ~2.8 nm at 532 nm). There are much larger changes in the Raman signals. In particular, the temperature effect increases strongly in the water vapor channel as the passband width decreases. For example, the ratio of transmitted intensities changes by more than 10% between 200 K and 300 K for a passband width less than ~12 cm^{-1} (~0.2 nm at 407.5 nm). By contrast the temperature sensitivity of the diatomic molecules O_2 and N_2 decreases for passband widths less than ~75 cm^{-1} (~1 nm at 375.4 nm and ~2.5 nm at 580.4 nm) and ~100 cm^{-1} (~1.5 nm at 386.7 and ~3.7 nm at 607.8 nm), respectively, where peak percentage changes of 3.3% and 1.8% occur, respectively. This reflects the fact that, for measurements of Raman vibrational spectra from diatomic molecules such as nitrogen and oxygen, as a passband that is centered on the q-branch of the Raman feature becomes more narrow, increasingly fewer of the vibrational-rotational lines will be transmitted thus reducing the temperature dependent effect.

Table 1 and figure 3 reveal a stronger temperature sensitivity for the water vapor signal than the other Raman signals. This results from the more complex, non-symmetric nature of the water vapor spectrum. It is interesting to consider the effect of different combinations of water vapor passband width and center location on the percentage change in transmitted intensity between 200K and 300K. Figure 4 shows the ratio of transmitted intensity for water vapor passbands with FWHM up to 50 cm^{-1} (~1 nm at 407.5 nm) and central locations varying between 3649 and 3656 cm^{-1} (407.45 nm and 407.56 nm). This figure reveals that the ratio of transmitted intensities is strongly dependent on the exact center location for the water vapor passband. For example, the transmitted intensity of a 18 cm^{-1} (~0.3 nm) passband centered at 3656 cm^{-1} (407.56 nm) would change by ~8% between 200 K and 300 K. If this passband is determined primarily by an interference filter, then tilting the filter by ~1 degree (assuming a filter effective index of refraction of ~1.5) [49] to center it at 3649 cm^{-1} (407.43 nm) would essentially eliminate the temperature sensitivity. The total range of passband center location plotted in figure 3 is only 1.2 Å for excitation at 354.7 nm. This indicates that spectral transmission data with accuracy of ~0.1Å are needed to assess the temperature dependence of very narrowband water vapor measurements with confidence.

4.4 Temperature dependent functions versus altitude

As an illustration of how to apply the temperature corrections, the profiles of $F_R(r), F_N(r), F_O(r)$ and $F_H(r)$ have been evaluated assuming the U.S. Standard Atmosphere [50] temperature profile and filter widths in cm^{-1} that correspond to 0.3 nm and 2.0 nm for excitation at 354.7 nm. The results are presented in figure 5. Again, $F_X(r)\ d\sigma_X(\pi)/d\Omega$ quantifies the effective cross section for molecule X due to changes in transmission over the passband. The narrower passbands transmit less of the rotational or vibrational-rotational Raman lines and thus less of the total cross section. In the case of O_2, the fraction of total cross section that is present in the vibrational-rotational lines is larger than for N_2 and thus, for comparable passband widths, $F_O(r)$ has a smaller value than $F_N(r)$.

4.5 New formulation of the single scattering Lidar equations containing temperature sensitivity

Using simplified formulations of the temperature sensitivity as in equation 6, the single-scattering Rayleigh-Mie and Raman lidar equations can now be expressed as follows

$$\begin{aligned} P\left(\Delta\lambda_R, r\right) &= \frac{O_R\left(r\right)\ P_0\left(\lambda_L\right)\ A\,\xi\left(\lambda_L\right)\left(F_R(T\left(r\right))\beta_\pi^{mol}\left(\lambda_L, r\right) + \beta_\pi^{aer}\left(\lambda_L, r\right)\right)}{r^2} \\ &\times \exp\left(-2\int_0^r \alpha(\lambda_L, r^{'})dr^{'}\right) \end{aligned} \tag{7}$$

$$\begin{aligned} P\left(\Delta\lambda_X, r\right) &= \frac{O_X\left(r\right)\ F_X(T\left(r\right))\ P_0\left(\lambda_L\right)\ A\,N_X\left(r\right)\ \frac{d\sigma_X(\pi)}{d\Omega}\ \xi\left(\lambda_X\right)}{r^2} \\ &\times \exp(-\int_0^r \{\alpha(\lambda_L, r^{'}) + \alpha(\lambda_X, r^{'})\}dr^{'}) \end{aligned} \tag{8}$$

where $\beta_\pi^{mol}\left(\lambda_L, r\right) = N_R\left(r\right)\ d\sigma_R\left(\pi\right)/d\Omega$ and $d\sigma_R\left(\pi\right)/d\Omega$ is the full Rayleigh cross section including the effects of rotational Raman scattering, the passband peak transmissions are given by the efficiency terms $\xi\left(\lambda_X\right)$. Notice that in the Rayleigh-Mie equation, the temperature dependent term $F_R(T\left(r\right))$ multiplies only $\beta_\pi^{mol}\left(\lambda_L, r\right)$ and not $\beta_\pi^{aer}\left(\lambda_L, r\right)$ since only the molecular cross section exhibits the temperature dependence considered here. These forms of the lidar equations will be used in the derivations to come after carefully considering the calculation of the transmission terms in the lidar equations.

4.6 The atmospheric transmission function

The atmospheric transmission function for the Raman lidar equation, $\exp[-\int_0^r \{\alpha(\lambda_L, r^{'}) + \alpha(\lambda_X, r^{'})\}dr^{'}]$, accounts for the fact that photons are transmitted into the atmosphere at the laser wavelength, λ_L, and return at the Raman shifted wavelength, λ_X, for Raman species X. (The Rayleigh-Mie case is obtained simply by setting $X = L$.) Since the atmospheric extinction is different at these wavelengths, the transmission factor must account for this. The extinction that occurs at a certain wavelength is, in general, due to both scattering and absorption from both aerosols and molecules in the atmosphere. The total extinction coefficient is therefore given by aerosol and molecular contributions

$$\alpha(\lambda, r) = \alpha_{aer}\left(r\right) + \sum_{i=1}^{M} N_i\left(r\right)\left[\sigma_i\left(\lambda\right) + \eta_i\left(\lambda\right)\right] \tag{9}$$

In this equation, $\alpha(\lambda, r)$ is the total extinction at wavelength λ and range r, $\alpha_{aer}(r)$ is the extinction due to aerosol scattering and absorption, $N_i(r)$ is the molecular number density of the i^{th} scatterering/absorbing molecular species, $\sigma_i(\lambda)$ is the total scattering cross section for the i^{th} molecular species and $\eta_i(\lambda)$ is the absorption cross section for the i^{th} molecular species. M is the total number of the different molecular species being considered. The use of a XeCl excimer laser (~308 nm) as output source requires the use of 9 due to significant ozone absorption of the outgoing beam in both the troposphere and stratosphere [51]. For various other choices of output wavelength, molecular absorption is usually negligible. For example, a Raman lidar using a UV laser such as a XeF excimer (351 *nm*) or a frequency-tripled Nd:YAG (355 *nm*), the wavelength range of the return signals is approximately 350 - 410 *nm*, a region of the spectrum where molecular absorption is negligible [52]. The fundamental wavelength from the doubled Nd:YAG (~532 nm) and the Raman shifted wavelengths for oxygen (~580 nm) and nitrogen (~608 nm) also are not absorbed significantly below the stratosphere. However, measurements at these wavelengths through the stratopheric ozone layer are attenuated due to ozone by approximately 2-4% (tropospheric ozone absorption is negligible at these wavelengths due to the much lower abundance of ozone in the troposphere than the stratosphere). The Raman shifted wavelength for water vapor when excited at ~532 nm is ~661 nm. Stratospheric ozone also absorbs by ~1-2% here as well, but there is also weak absorption due to water vapor. For the standard tropical atmosphere of water vapor [50], absorption through the entire atmospheric column is ~1%. For drier atmospheres the absorption will be less. Therefore, for Rayleigh-Mie or Raman measurements of oxygen, nitrogen and water vapor using a XeF excimer or tripled Nd:YAG lasers and for Rayleigh-Mie and Raman measurements of oxygen and nitrogen below the stratosphere using the doubled Nd:YAG laser, the molecular component of the atmospheric extinction coefficient $\alpha(\lambda, r)$ is due only to scattering by the various molecules in the atmosphere and the following equation for the extinction coefficient applies

$$\alpha(\lambda, r) = \alpha_{aer}(r) + \sum_{i=1}^{M} N_i(r)\,\sigma_i(\lambda) \tag{10}$$

Typical Rayleigh scattering formulas provide a composite cross section for the collection of molecules that make up normal air. Using this fact to re-express the equation yields

$$\alpha(\lambda, r) = \alpha_{aer}(r) + N_{air}(r)\,\sigma_{air}(\lambda) \tag{11}$$

for the atmospheric extinction when absorption is not an issue. Equation 9 should be used to account for molecular absorption for the other Raman lidar measurements discussed here: 1) when using a 308 nm laser source, 2) for measurements through the stratospheric ozone layer using a ~350 nm source, and 3) for Raman water vapor measurements using a doubled Nd:YAG (532 nm).

5 Atmospheric extinction due to molecules and aerosols

In order to evaluate the atmospheric transmission function, we need to evaluate separately the contributions due to molecular and aerosol extinction. The calculation of molecular extinction and optical depth has been thoroughly discussed elsewhere including the effects of the dispersion of polarization [53] [54]. However, since some of the common formulas for Rayleigh extinction that are typically used in the lidar field [34] either do not account for depolarization at all or neglect its dispersion with wavelength, the calculation of molecular extinction will first be reviewed here after which the calculation of aerosol extinction will be discussed.

5.1 Molecular extinction and backscattering including the effects of polarization

In the absence of absorption, extinction of the laser beam is entirely due to scattering. Equations 12 through 14 are used to calculate the cross section per molecule for Rayleigh scattering [30] [53] [54] .

$$\sigma(\lambda) = \frac{24\pi^3 \left(n_s^2(\lambda) - 1\right)^2}{\lambda^4 N_s^2 \left(n_s^2 + 2\right)^2} F_K(\lambda) \tag{12}$$

$$n_s(\lambda) = 10^{-8}\left(\frac{5791817}{238.0185 - (1/\lambda)^2} + \frac{167909}{57.362 - (1/\lambda)^2}\right) + 1 \tag{13}$$

$$F_K(\lambda) = \left(\frac{6 + 3\rho_0^t(\lambda)}{6 - 7\rho_0^t(\lambda)}\right) \tag{14}$$

where $\sigma(\lambda)$ is the cross section per molecule at the wavelength λ, $n_s(\lambda)$ is the empirical formula [55] for the real refractive index for dry air at standard temperature and pressure (STP) at wavelengths greater than 230 nm [54], N_s is the molecular number density for air at STP (2.547 x 10^{19} cm^{-3}), $F_K(\lambda)$ is the King factor shown defined in terms of, ρ_0^t, the total (Rayleigh + rotational Raman) depolarization from a natural light source [30], the value of which is determined by the magnitudes of the parallel and perpendicular components of the dynamic polarizability [53] $\alpha^{\|}(\lambda)$ and $\alpha^{\perp}(\lambda)$ as follows:

$$\begin{aligned} \rho_0^t(\lambda) &= \frac{6\epsilon(\lambda)}{45 + 7\epsilon(\lambda)} \qquad (15) \\ \epsilon(\lambda) &= 3\frac{\alpha^{\|}(\lambda) - \alpha^{\perp}(\lambda)}{\alpha^{\|}(\lambda) + 2\alpha^{\perp}(\lambda)} \qquad (16) \end{aligned}$$

For example, $\rho_0^t(\lambda)$ changes from 0.0357 to 0.0273 over the range 250-1000 nm. So it clear that the pertinent depolarization quantity ρ_0^t has a wavelength dependence that influences the Rayleigh scattering cross section. Also, due to the random distribution of molecules in the atmosphere, the cross section given by equation 12 is valid regardless of laser polarization.

5.1.1 Comparison of different formulations of Rayleigh cross section

The dispersion of depolarization must be included for an accurate determination of Rayleigh cross section as a function of wavelength [54]. Some calculations of Rayleigh cross section either neglect the dispersion of depolarization or omit the King factor completely [34]. Figure 6 compares these different methods of calculating the Rayleigh cross section. Figure 6 compares two approximate methods of calculating the Rayleigh cross section with the full calculation using equation 12. The first approximate calculation uses equation 12 but with a constant value for depolarization, chosen here to be 0.0279 [29], the second method neglects the King factor completely. As the figure shows including the dispersion of polarization changes the Rayleigh cross section by more than 1% across the wavelength range of 250 - 800 nm when compared with the wavelength independent depolarization assumption. Neglecting the King factor yields a Rayleigh optical depth approximately 5% larger than actual.

The total Rayleigh volume-scattering coefficient (in units of, for example, km^{-1}) as a function of wavelength at standard temperature and pressure (STP) is now given by [54]

$$\beta_s = N_s \sigma(\lambda) \tag{17}$$

For any pressure, temperature or number density, the Rayleigh volume scattering coefficient may be determined from [54]

$$\beta^{mol}(\lambda, r) = N(r)\,\sigma(\lambda) = \beta_s(\lambda)\frac{N(r)}{N_s} = \beta_s(\lambda)\frac{P(r)}{P_s}\frac{T_s}{T(r)} \tag{18}$$

where β_s, P_s and T_s are calculated at STP. In the absence of absorption, molecular extinction is determined completely by Rayleigh scattering and thus the molecular component of the atmospheric extinction coefficient $\alpha(\lambda, r)$, from equation 11, is given by equation 18. The notation for the volume scattering coefficient, $\beta^{mol}(\lambda, r)$, is not to be confused with the previously defined backscatter coefficient, $\beta_{\pi}^{mol}(\lambda, r)$. It is convenient at this point to describe the calculation of the Rayleigh backscatter coefficient.

5.1.2 Calculation of Rayleigh backscatter coefficient

To calculate the Rayleigh backscatter coefficient, the following formulation will be used [54]

$$\beta_a^{mol}(\theta, \lambda, r) = \frac{\beta^{mol}(\lambda, r)}{4\pi} P_{Ray}\left(\theta, \rho_0^t(\lambda)\right) \tag{19}$$

where $\beta_a^{mol}(\theta, \lambda, r)$ is the Rayleigh angular volume-scattering coefficient (in units of, for example, $km^{-1}sr^{-1}$). The backscattering case, of such special importance to lidar, has been given its own notation of $\beta_a^{mol}(\theta, \lambda, r) = \beta_{\pi}^{mol}(\lambda, r)$. Other than the 4π normalization factor, the right hand side of this equation consists of two terms: 1) $\beta^{mol}(\lambda, r)$, the Rayleigh volume scattering coefficient given by equation 18 and 2) $P_{Ray}\left(\theta, \rho_0^t(\lambda)\right)$, the scattering amplitude as a function of angle, which is equal to [56]

$$P_{Ray}\left(\theta, \rho_0^t(\lambda)\right) = \frac{3}{2\left(1 + \rho_0^t(\lambda)\right)}\left[\left(1 + \rho_0^t(\lambda)\right) + \left(1 - \rho_0^t(\lambda)\right)\cos^2\theta\right] \tag{20}$$

where $\rho_0^t(\lambda)$ is the Rayleigh depolarization factor defined earlier. The Rayleigh backscattering coefficientis obtained simply by setting $\theta = \pi$ in the equations 19 and 20. The formulation of the Rayleigh scattering phase function given in equation 20 is from Goody [56] and is in fact equivalent to the form given in Chandrasekhar [57] and Bucholtz [54]. However, Goody's form is expressed directly in terms of the depolarization of natural light, $\rho_0^t(\lambda)$,that appears in the King factor as opposed to a term that Chandrasekhar and Bucholtz refer to as $\gamma(\lambda) = \rho_0^t(\lambda)/(2-\rho_0^t(\lambda))$, which is equivalent to the term $\rho_v^t(\lambda)$ defined by Young [29] as the depolarization of incident light polarized normal to the scattering plane.

It is interesting to compare the formulation of Rayleigh backscattering coefficient in equation 19 to a simpler numerical version that is common in the lidar literature but that does not account for the effects of the dispersion of depolarization. The simpler equation is [34]

$$\beta_\pi^{simpler}(N,\lambda) = N\,5.45\left[\frac{550}{\lambda(nm)}\right]^4 \times 10^{-28} \quad (cm^{-1}sr^{-1}) \tag{21}$$

where N is the molecular number density in units of cm^{-3}. Figure 7 shows the ratio of equations 21 and 19 over a range of 250 to 1000 nm where the latter equation has been evaluated at an angle of π.

The two methods differ by more than 10% for wavelengths shorter than approximately 280 nm and by more than 5% for wavelengths greater than approximately 800 nm. In the range of 350 nm, where the popular Raman laser sources of the tripled Nd:YAG and the XeF excimer have their output, the simpler formulation is ~3% smaller than the full treatment given in equation 19 whereas in the vicinity of 530 nm, the simpler treatment is now ~3% larger. These are significant differences implying that the complete formulation of Rayleigh backscatter coefficient given by equation 19 should be used instead of simpler formulations such as that in equation 21.

5.2 Aerosol extinction

To compute aerosol extinction analytically generally requires knowledge of the exact nature of the aerosols that are responsible for the extinction. Given the size distribution of the aerosols as a function of range and both real and imaginary indices of refraction, a calculation using Mie theory can be performed that will estimate the extinction as a function of range. This can be done very accurately for non-precipitating cloud water droplets, which are spherical, provided that multiple scattering is not significant. But for other aerosols, which can have irregular shapes that are usually not known, calculations of aerosol scattering properties using Mie theory are approximations at best.

However, with the Raman lidar, another approach to the calculation of aerosol extinction is possible. The Raman vibrational [58] (or the pure rotational [39]) signal from nitrogen or oxygen may be used to calculate the round-trip atmospheric extinction , which for vibrational Raman scattering occurs at the laser wavelength for the outgoing path and at the Raman shifted wavelength for the return path.

5.2.1 Development of the extinction equations including the effects of temperature sensitivity

Aerosol extinction can be quantified in a direct manner by using either the Raman nitrogen or oxygen signals [58] [9]. At the ultra-violet and visible wavelengths of the lasers typically used in Raman lidar systems, atmospheric absorption is negligible so aerosol extinction is determined by the total amount of light scattered into all directions. This is the integral of the aerosol scattering intensity as a function of angle (the phase function) and quantifies an important radiative property of the aerosols. The equation for calculating aerosol extinction using the temperature dependent Raman lidar data can be derived along similar lines as in Ansmann et. al. [58]. Assuming the use of the Raman nitrogen signal for the calculation of aerosol extinction, the result is

$$\begin{aligned} &\alpha_{aer}(\lambda_L, r) + \alpha_{aer}(\lambda_N, r) \\ =\ &\frac{d}{dr}\left[\ln\left(\frac{O_N(r)\ F_N(T(r))\ N_N(r)}{r^2\ P(\lambda_N, r)}\right)\right] - \alpha_{mol}(\lambda_L, r) - \alpha_{mol}(\lambda_N, r) \end{aligned} \tag{22}$$

where $\alpha_{aer}(\lambda_L, r)$ is the extinction due to aerosols on the outgoing path at the laser wavelength, $\alpha_{aer}(\lambda_N, r)$ is the aerosol extinction on the return path at the Raman shifted wavelength, $\alpha_{mol}(\lambda_L, r)$ is the molecular extinction at the laser wavelength, and $\alpha_{mol}(\lambda_N, r)$ is the molecular extinction at the Raman shifted wavelength.

Equation 22 is the fundamental Raman lidar aerosol extinction equation. It is identical to the results of Ansmann et. al. [58] except for the inclusion of the temperature dependent factor $F_N(T(r))$. The atmospheric number density is required to evaluate this equation both for the calculation of the molecular extinction terms (through the use of equation 18) as well as to evaluate the number density $N_N(r)$. In the lowest ~100 km of the atmosphere the total atmospheric density is proportional to $N_N\left(r\right)$ and thus gives identical results in the equation. The sensitivity of Raman measurements of aerosol extinction to changes in atmospheric temperature and density variations has been studied by Ansmann et. al. [58]. Their conclusion was that the use of a standard atmospheric model for calculating molecular extinction can introduce significant errors in aerosol extinction when the aerosol loading is very low. Therefore the more accurate molecular number density profile available from a radiosonde is recommended under such conditions.

Equation 22 indicates that the fundamental quantity that can be evaluated using a Raman lidar is the two-way extinction that occurs along the round-trip path from the laser to a scattering element and back to the telescope. In order to translate this into one-way extinction at a single wavelength, knowledge of the wavelength scaling of aerosol extinction is needed. The scaling of aerosol extinction may be handled as follows [59]

$$\frac{\alpha_{aer}(\lambda_L, r)}{\alpha_{aer}(\lambda_N, r)} = \left(\frac{\lambda_N}{\lambda_L}\right)^{k(r)} \tag{23}$$

where $k\left(r\right)$ may vary between approximately 0 and 2 depending on the nature of the aerosols [9] and is a function of range. Using equation 23, the expression for aerosol extinction at the laser wavelength becomes

$$\alpha_{aer}(\lambda_L, r) = \frac{\frac{d}{dr}\left[\ln\left(\frac{O_N(r)\, F_N(T(r))\, N_N(r)}{r^2\, P(\lambda_N, r)}\right)\right] - \alpha_{mol}(\lambda_L, r) - \alpha_{mol}(\lambda_N, r)}{1 + \left(\frac{\lambda_L}{\lambda_N}\right)^{k(r)}} \tag{24}$$

An alternate form of this equation, which is preferred since it allows quantities to retain their original statistical distributions when determining the numerical derivative [60] is

$$\alpha_{aer}(\lambda_L, r) = \frac{\begin{array}{c}\frac{1}{O_N(r)}\frac{d}{dr}O_N\left(r\right) + \frac{1}{F_N(T)}\frac{d}{dr}F_N(T\left(r\right)) + \frac{1}{N_N(r)}\frac{d}{dr}N_N\left(r\right) \\ -\frac{1}{r^2 P(\lambda_N, r)}\frac{d}{dr}[r^2 P\left(\lambda_N, r\right)] - \alpha_{mol}(\lambda_L, r) - \alpha_{mol}(\lambda_N, r)\end{array}}{1 + \left(\frac{\lambda_L}{\lambda_N}\right)^{k(r)}} \tag{25}$$

As described in reference [60], the technique of least squares fitting assumes that the data to be regressed are normally distributed. The use of equation 25 permits all quantities being regressed to retain their original statistical distributions, which are assumed to be Gaussian or near-Gaussian. This equation, therefore, is preferred to equation 24 for evaluating aerosol extinction since the ratio of two Gaussian distributed quantities is not Gaussian.

In principle, equation 25 can be used over the entire range of the lidar profile to evaluate the aerosol extinction. However, in practice it is quite difficult to quantify the lidar channel overlap function sufficiently well to apply equation 25 in the overlap region. This is due to the fact that the derivative of the natural logarithm of the overlap must be evaluated. In the overlap region, the signal may be changing very rapidly so that small errors in quantifying the overlap function can introduce large errors in the derived aerosol extinction. For this reason calculations of aerosol extinction are typically performed on the portion of the lidar profile that is fully overlapped, i.e. where $O_N(r) = 1$. It should be noted as well that since the extinction will typically be evaluated over relatively short ranges (i.e. dr will in general be on the order of 100 meters) that the factor $F_N(T(r))$ will have little influence since, as can be seen in figure 5, its change is insignificant over such short ranges. This is the case in the normal atmospheric since $F_N(T(r))$ is not a strong function of range. For measurements of extinction in a smoke stack or in the vicinity of flames this would not be the case, however, and the factor $F_N(T(r))$ could change over short ranges and influence the extinction calculation.

Before evaluating equation 25 for the case of tropospheric aerosols, the possible influence of multiple scattering on these measurements must be addressed. Tropospheric aerosols, excluding cloud particles, range in size from less than 0.1 μm in radius up to 10 μm and larger in some cases [61]. The multiple scattering due to aerosols in this size range is studied in appendix 1. The simulations performed there indicate that multiple scattering is likely to be negligible for boundary layer extinction measurements. However, for elevated desert dust layers multiple scattering may have a small but noticeable effect on the calculation of extinction.

5.2.2 Evaluation of the extinction equation

The evaluation of equation 25 appears to be rather straightforward once all the required quantities are known. However, the derivative term actually presents subtle and quite important difficulties relating to the proper statistical evaluation of a derivative (or slope) in the case of a lidar profile, which is not a continuous function. The statistical rules pertaining to determining the best mathematical model for fitting a set of data can be applied with good result [60] both for the evaluation of the extinction and the error in extinction.

5.2.3 Example aerosol extinction profile

An example of aerosol extinction computed from data acquired by the NASA/GSFC Scanning Raman Lidar (SRL) during the third Convection and Moisture Experiment (CAMEX-3) [8] on the night of August 26, 1998 at Andros Island, Bahamas is shown in figure 8. At the time of this field campaign, the SRL used a XeF excimer laser (351 nm), 0.76 m telescope and high and low range photomultiplier tubes for each of the Rayleigh-Mie, oxygen, nitrogen and water vapor signals [5]. The results shown were obtained from the raw Raman lidar measurement of molecular nitrogen by first correcting for the finite photon counting bandwidth, subtracting the background and then applying equation 25. For reference, various photon counting correction techniques are reviewed in appendix 2.

The aerosol extinction profiles shown use a 20-minute summation of data. The molecular extinction coefficients were derived using equation 18 and the atmospheric density that was measured by a radiosonde launched that night. In the figure, the influence of the aerosol scaling parameter, k (known as the Angstrom coefficient), is also tested. Figure 8 shows a typical aerosol profile from Andros Island during the CAMEX-3 campaign. The values of extinction below ~0.25 km are influenced by the lidar overlap function. Changing the Angstrom coefficient (considered constant with range) from k=0 to k=2 increases the aerosol extinction values by approximately 8%. It has the same effect on the aerosol optical depth between 0.25 and 3 km which may be calculated by simply integrating the extinction curve over this altitude range. Using k=1, the aerosol optical thickness (at 351 nm) between 0.25 and 3 km was approximately 0.13 for this example.

The uncertainty in the Angstrom coefficient can be reduced by using coincident sun photometer data, although the sun photometer only provides a column average value while the lidar is measuring the profile of aerosols. The uncertainty in the Angstrom coefficient determined using a sun photometer is a function of the wavelength interval used to determine the coefficient, the aerosol optical depth and the quality of the calibration of the instrument in use. In general, for instruments in the NASA/GSFC AERONET (http://aeronet.gsfc.nasa.gov:8080/), uncertainty in Angstrom coefficient will be less than ±0.2 for the 340-380 nm wavelength interval if the aerosol optical thickness is greater than 0.4 [62] [63]. It is interesting to note that due to the existence of an AERONET reference standard at NASA/GSFC, a ±0.2 uncertainty in Angstrom coefficient is obtained for measurements made there when aerosol optical depths are greater than 0.2 [64]. It is estimated that uncertainty in the value of $k\,(r)$ contributes an error of less than 5% to the aerosol extinction measurements shown in figure 8.

The aerosol optical depth of ~0.13 in the current example implies that approximately 12% of the light was scattered from the beam due to aerosols ($e^{-0.13} \cong 0.88$). These measured values of aerosol extinction in the UV can be used to estimate the horizontal visibility experienced by ground-based observers. The "visual range" may be estimated from the empirical formula [34]

$$\alpha(\lambda) \approx \frac{3.91}{R_v} \left\{ \frac{550}{\lambda(nm)} \right\}^k \; (km^{-1}) \tag{26}$$

where α is the total atmospheric extinction coefficient and R_v is the visual range. At visible wavelengths and under most aerosol loading conditions, aerosol extinction is the dominant source of atmospheric attenuation [34]. For example, near the surface in figure 8, aerosol extinction at 351 nm was approximately 0.1 km^{-1}. Scaling this value to 550 nm using equation 23 and $k = 1$ yields an aerosol extinction at 550 nm of approximately 0.06 km^{-1}. By contrast, molecular extinction under standard temperature and pressure conditions, using equation 17 is approximately 0.01 km^{-1}. Using these values in equation 26, yields a value of visual range in excess of 50 km. The aerosol loading present on August 26 was typical for Andros Island during CAMEX-3 implying that aerosol optical depths were low and visibilities were generally very good.

This example demonstrates that the aerosol optical depth is an important parameter than influences visibility and thus radiative transfer. As demonstrated above, the optical depth can be determined by integrating the aerosol extinction profile. When calculating the optical depth in this manner, however, errors at all levels in the extinction profile must be added together to determine the error budget for the optical depth calculation. This can result in a larger uncertainty in the determination of the optical depth than the more straightforward calculation which will now be presented.

5.2.4 Aerosol optical depth

Integrating both sides of equation 22 over the range $\{r_1, r_2\}$ yields the two way aerosol optical depth between r_1 and r_2 :

$$
\begin{aligned}
& \int_{r_1}^{r_2} [\alpha(\lambda_L, r) + \alpha(\lambda_N, r)] \ dr \\
= \ & \left[\ln \left(\frac{O_N(r) \ F_N(T(r)) \ N_N(r)}{r^2 \ P(\lambda_N, r)} \right) \right]_{r_1}^{r_2} - \int_{r_1}^{r_2} [\alpha_{mol}(\lambda_L, r) + \alpha_{mol}(\lambda_N, r)] \ dr \\
= \ & \ln \left(\frac{O_N(r_2) \, F_N(T(r_2)) \ N_N(r_2) \, r_1^2 \ P(\lambda_N, r_1)}{O_N(r_1) \, F_N(T(r_1)) \ N_N(r_1) \, r_2^2 \ P(\lambda_N, r_2)} \right) - \int_{r_1}^{r_2} [\alpha_{mol}(\lambda_L, r) + \alpha_{mol}(\lambda_N, r)] \ dr \qquad (27)
\end{aligned}
$$

The use of equation 27 to calculate aerosol optical depth eliminates the need to perform a derivative of the lidar signal. This simplifies calculations when all that is needed is the mean value of extinction through a layer such as is required to calculate optical depth of the layer.

The error in the aerosol optical depth has both random and systematic components. The systematic part of the error is in general difficult to evaluate since it requires knowledge of the absolute value of the quantity being measured. However, because the values of density and temperature that one uses in the evaluation of equation 27 would likely come from a single model profile or radiosonde measurement, there is likely to be a systematic component to the errors in $F_N(T(r))$, $N_N(r)$, and $\alpha_{mol}(\lambda_L, r)$. It is clear from equation 27 that the systematic component of errors in $F_N(T(r))$ and $N_N(r)$ will tend to cancel due to the ratio inside of the logarithm. However, a systematic error in density of a certain percentage would have the same percentage effect on the calculated molecular optical depth. As mentioned earlier, this effect was considered by Ansmann et. al. [58] where they concluded that radiosonde measurements of density are preferred over model values in the evaluation of equation 27 for small aerosol optical depths.

The random component of the error in optical depth may be calculated using standard error propagation formulas [65] and is given by

$$\sigma^2_{AerosolOD} \simeq \frac{\sigma^2_{O_N(r_2)}}{O_N^2(r_2)} + \frac{\sigma^2_{O_N(r_1)}}{O_N^2(r_1)} + \frac{\sigma^2_{F_N(T(r_2))}}{F_N^2(T(r_2))} + \frac{\sigma^2_{F_N(T(r_1))}}{F_N^2(T(r_1))} + \frac{\sigma^2_{N_N(r_2)}}{N_N^2(r_2)} + \frac{\sigma^2_{N_N(r_1)}}{N_N^2(r_1)} + \frac{\sigma^2_{P(\lambda_N,r_2)}}{P^2(\lambda_N,r_2)} + \frac{\sigma^2_{P(\lambda_N,r_1)}}{P^2(\lambda_N,r_1)} + 2\sigma^2_{MolecularOD} \tag{28}$$

where, to be clear, $\sigma^2_{AerosolOD}$ refers to the variance of the two-way aerosol optical depth and $\sigma^2_{MolecularOD}$ refers to the variance of the one-way molecular optical depth. If $F_N(T(r))$ varies little over the range of the optical depth calculations, such as in the normal atmosphere, it should contribute at most a small amount to the total error. In a smoke stack or in flames, this may not be the case. Thus, $F_N(T(r))$ can be considered negligible over ranges where the temperature does not change appreciably. Therefore, if the temperature changes slowly over the range being considered and, furthermore, if the calculation is done outside the region where the overlap function is an influence, the error equation reduces to

$$\sigma^2_{AerosolOD} \simeq \frac{\sigma^2_{N_N(r_2)}}{N_N^2(r_2)} + \frac{\sigma^2_{N_N(r_1)}}{N_N^2(r_1)} + \frac{\sigma^2_{P(\lambda_N,r_2)}}{P^2(\lambda_N,r_2)} + \frac{\sigma^2_{P(\lambda_N,r_1)}}{P^2(\lambda_N,r_1)} + 2\sigma^2_{MolecularOD} \tag{29}$$

The error in the radiosonde density data will determine the error budget for three of the terms above. Also, for a lidar system such as the SRL that uses photon counting data acquisition, Poisson statistics applies so that the variance in a measurement equals the accumulated number of counts of the measurement itself. Putting these together yields

$$\sigma^2_{AerosolOD} \simeq \frac{1}{P(\lambda_N,r_2)} + \frac{1}{P(\lambda_N,r_1)} + 4\ RadErr^2 \tag{30}$$

where $RadErr$ indicates the fractional random error in the radiosonde density measurement.

The equations are now developed for the two-way particle optical depth. If one desires to determine the one-way particle optical depth, it is necessary to use equation 23 to handle the wavelength scaling. The appropriate error equation is this case is approximately one-half of equation 30 depending on the value of $k(r)$ used in equation 23. This completes the description of numerous calculations required to evaluate the lidar equation. Now the meteorological quantities of water vapor mixing ratio, aerosol scattering ratio and aerosol backscatter coefficient may be derived by considering ratios of Raman lidar signals. This will be covered in part II [28] of this paper.

6 Summary

As the number of Raman water vapor and aerosol lidar systems in use in the world has been on the increase recently, particularly in Europe, it seemed an appropriate time to undertake an updated evaluation of the traditional Raman lidar water vapor and aerosol technique including effects such as the temperature dependence of Raman scattering. Toward that end, this paper is part one of a thorough two-part review of the traditional, single-laser-wavelength, Raman lidar technique for measuring atmospheric water vapor and aerosols. In this paper, a detailed study of the evaluation of both the Rayleigh-Mie and Raman lidar equations has been presented including the effect of the temperature sensitivity of both rotational and vibrational-rotational Raman scattering. New forms of the Rayleigh-Mie and Raman lidar equations were developed that permit the temperature sensitivity of these equations to be considered as a multiplicative factor times the traditional lidar equations. These temperature dependent factors were calculated for Rayleigh, Raman nitrogen, oxygen and water vapor signals using different passband widths and center positions. The Raman water vapor simulations were performed using recent results that permit the full OH-stretch mode of water vapor to be simulated. These calculations indicated a greater than 6% change in transmitted intensity for the water vapor signal between 200 K and 300 K for a $0.3\ nm$ filter centered at 3654 cm^{-1}. Furthermore, the temperature dependence of the water vapor signal for a narrow passband is highly sensitive to the exact filter spectral location. The calculations also indicated that the influence of the temperature sensitivity of the pure rotational Raman lines on the Rayleigh signal is generally much less than 1% while the Raman nitrogen can change by nearly 2% and that of oxygen by more than 3% over the same temperature range. The calculation of atmospheric transmission was discussed in detail. Differences up to 5% were found in calculations of molecular extinction due to the effects of the dispersion of depolarization. A simple formulation of Rayleigh backscattering that is commonly used in the lidar field was found to differ significantly from the full calculations that are suggested here. Temperature dependent aerosol extinction and optical depth equations were presented. The influence of the wavelength scaling of aerosols was considered in these calculations. In appendices, the influence of multiple scattering was considered for boundary layer and elevated aerosol layers. It was found that multiple scattering due to elevated dust layers can significantly effect the calculation of extinction using certain lidar configurations. Correction techniques for photon counting pulse pileup were reviewed. In part II [28], the temperature dependent equations developed here will be used to derive new forms of the ratio equations for Raman lidar water vapor and aerosol analysis.

7 Acknowledgements

Support for this activity has come from the NASA Dynamics and Remote Sensing and Radiation Sciences programs as well as the Department of Energy's Atmospheric Radiation Measurements program. The author is grateful to J. M. Fernandez for the helpful conversations concerning the modeling of the Raman water vapor spectrum.

1 Appendix: The Influence of Multiple Scattering on Tropospheric Aerosol Extinction Measurements

For light scattered by particles of the same dimension or larger than the wavelength of the incoming light, as the particle size increases, forward-scattered light is confined to an increasingly narrow angular cone. This makes it more likely that a photon that is scattered forward in a first scattering event will interact with another particle in a second scattering event and be backscattered within the field of view of the lidar receiver.

The lidar equations formulated earlier were for single scattering only. Therefore, in the case of scattering involving large particles where multiple scattering is more likely to occur, the use of the single scattering equations can lead to errors in the calculated quantities. Most of the quantities derived from Raman lidar data are based on ratios of lidar signals so that the multiple scattering influence tends to cancel in the ratio [66]. Examples of these quantities are the water vapor mixing ratio, liquid water mixing ratio, aerosol scattering ratio and the aerosol backscatter coefficient. However, aerosol extinction and optical depth are calculated using only a single lidar signal (e.g. Raman nitrogen) which, in the case of large particles, can be significantly influenced by multiple scattering.

The influence of multiple scattering on lidar signals is related to the optical depth of the scattering medium, the size of particles that are doing the scattering, the range to the scattering volume, the laser divergence and the telescope field of view. The formulation developed by Eloranta [67] will be used here to study this influence assuming 1 mrad laser divergence and 2 mrad telescope field of view. A description of the equations used here has been published recently for the case of Raman lidar measurements of cirrus cloud multiple scattering [8]. It is important to note that the modeling of multiple scattering in the case of the molecular (as opposed to the Rayleigh-Mie) signal is aided by the slowly varying nature of the molecular phase function in the backscatter direction [67]. By contrast, to simulate multiple scattering for the Rayleigh-Mie signal requires a knowledge of the profile of particle size since the Mie phase function changes rapidly near the exact backward direction.

1.1 Multiple scattering by tropospheric aerosols - boundary layer and elevated dust layers

Six synthetic profiles of aerosol extinction were created to study the influence of multiple scattering on the measurement of extinction using Raman lidar and are shown in figure 9. The boundary layer extinction profiles have aerosol optical depths of 0.375, 0.75 and 1.5, respectively, to simulate low, medium and high aerosol loading. The extinction profiles simulating elevated dust layers have optical depths of 0.1, 0.2, and 0.5.

Aerosols can range in size from much less than 1 micron (rural aerosols) to more than 10 microns (desert dust). Second order multiple scattering was calculated for the three boundary layer extinction profiles shown in figure 9 assuming that the aerosol particles were of constant radius throughout the profile where the radii chosen were 0.5 and 2.0 microns. The results are shown in figure 10 with the 0.5 micron calculations on the left and the 2.0 micron calculations on the right. The plot of the 2.0 micron results also includes the fractional error in the extinction as a function of range.

The multiple scattering due to 0.5 micron aerosols is considerably smaller than that for the 2 micron aerosol. Considering the 2 micron results shown on the right, it can be seen that at the peak of the high aerosol optical thickness case, the ratio of second order scattering to single scattering is less than 3%. The error in extinction due to second order multiple scattering is also plotted for the high optical depth case. The negative error is largest with a value of ~-1.5% at the surface where the aerosol layer is first encountered. It then increases toward zero at an altitude of ~1.5

km where the slope of the P_2/P_1 curve is zero. Above this altitude until the top of the aerosol layer, the error is positive reaching a maximum positive value of ~1.5% at the top of the layer. Since the optical depth is just the integral of extinction, the error in optical depth due to second order multiple scattering will be at most 1.5% as well. Third order scattering will be insignificant due to its much lower probability than second order scattering.

The Air Force Geophysics Lab (AFGL) marine oceanic aerosol model [61] peaks at 0.3 microns and predicts that there are only 51% and 1.8% as many particles of radii 0.5 and 2 microns, respectively as at the peak. For particles larger than 2 microns, the abundance drops exponentially. Therefore, due to the relative lack of large particles that these model calculations predict for tropospheric aerosols and the generally small effect that multiple scattering has on the calculation of boundary layer aerosol extinction, multiple scattering is unlikely to present a significant error source for boundary layer aerosols.

The same may not be the case for elevated layers of desert dust, which have been observed at large distances from their source regions [68] [69] [70] [71] and are characterized by preferential population of the coarse mode part of the distribution [72]. Keeping other parameters fixed, if the range to the scattering medium is increased the observed multiple scattering increases as well. This is due to the fact that a larger geometrical area is observed by a fixed field-of-view telescope as the range increases. Therefore one might expect that an elevated layer of aerosols would exhibit more multiple scattering than the same layer at lower altitudes. Furthermore, Dubovik et. al. [72] report aerosol mean radii of ~2.5 +/- 0.6 microns for sun photometer measurements of desert dust made over a period of approximately 2 years in Bahrain. Therefore, to study the possible influence of multiple scattering on extinction measurements of elevated desert layers, figure 11 shows multiple scattering calculations for a 1 km thick dust layer between 5 and 6 km with optical depth of 0.1, 0.25 and 0.5 using the elevated extinction profiles shown in figure 9. The aerosol size simulated is 3 microns. Both second and third order multiple scattering were used in these simulations. The error in extinction due to multiple scattering is also plotted for the 0.5 optical depth case. The figure shows that the peak ratio of multiple scattering to single scattering for the three optical depths is ~0.03, 0.07 and 0.14, respectively. The error in extinction for the 0.5 optical depth case is maximum and negative with a value of ~15% at the base of the aerosol layer. The error in extinction for the 0.25 optical depth case (not plotted) is approximately half of that for the 0.5

optical depth case or ~7% at the base. The error in extinction approaches zero at the top of the elevated layer. Above the layer where the influence of multiple scattering can still be seen, the derived aerosol extinction would be non-zero where in fact there are no aerosols. Therefore, the error in extinction is essentially infinite. This is an example of the phenomenon known as pulse-stretching that can be a significant issue for space-based lidar systems because of the enhancement of multiple scattering created by the large distance from the lidar system to the extinguishing layer. The difference in the behavior of the error in extinction between the boundary layer cases shown above and the elevated layers shown here are due mainly to the different profiles of extinction assumed. The conclusion based on this figure is that multiple scattering can become a significant error source in the calculation of extinction in elevated layers of desert dust.

2 Appendix: Photon pileup correction

Raman lidar systems frequently make use of photon counting data acquisition systems due to the weak nature of Raman scattering. For example, all of the data acquired by the SRL during the CAMEX-3 field campaign used photon counting electronics. Photon counting electronics have a certain minimum pulse pair resolution time which, in the case of the 100 Mhz DSP Technology units used in the SRL during CAMEX-3, was approximately 10 ns. The maximum measurable count rate corresponding to this is 100 MHz. However, this maximum count rate will be obtained only for a perfectly periodic input pulse train. The Raman lidar photon counting signals obey Poisson statistics and thus, for a certain mean count rate over a one-minute data acquisition time, the effective countrate for each laser pulse can vary significantly. For example, using a 1 μsec binwidth in the photon counters, a 40 MHz signal would correspond to 40 counts in a bin. The Poisson probability distribution for n counts with μ mean is given by

$$P(n,\mu) = \frac{e^{-\mu}\mu^n}{n!} \tag{B.1}$$

where $P(n,\mu)$ is the probability of measuring n counts in a time interval where the mean number of counts per time interval is μ. Figure 12 shows this distribution with mean of 40. From this figure, it is clear that the effective count rate of the signal from each laser pulse can deviate significantly from the 40 MHz average. Thus, from pulse to pulse, there is a varying probability that two pulses may arrive sufficiently closely spaced in time to be seen as a single event by the electronics.

Traditionally, there are two extremes of behavior that counting systems can exhibit. They are referred to as "paralyzable" and "non-paralyzable" [73]. A paralyzable counting system is one that is unable to provide a second output pulse unless there is a time interval of at least τ between two successive input pulses. If an additional pulse arrives during the response time τ, known as the deadtime, the deadtime of the apparatus is further extended by τ. In this way, at high count rates, the unit will be unable to respond and will be "paralyzed". Since the fraction of intervals that are longer than τ is given by $e^{-\tau N_{real}}$, the equation which relates the measured and true counting rates for a paralyzable counter is [73]

$$N_{measured} = N_{real} e^{-\tau N_{real}} \tag{B.2}$$

where $N_{measured}$ is the observed countrate and N_{real} is the actual countrate.

A non-paralyzable counter is one in which the response time τ is independent of the arrival of additional counts. In other words, a non-paralyzable counting system will asymptotically approach a maximum counting rate as the actual countrate increases. The equation describing the relationship of the measured countrate and the true countrate can be derived as follows. For an observed countrate of $N_{measured}$, the fraction of time that the counting unit is unable to respond to counts is $\tau N_{measured}$, since each observed count will produce a single deadtime period. Thus the fraction of time that the unit is sensitive to counts is $1 - \tau N_{measured}$. The measured countrate may then be expressed as [73]

$$N_{measured} = (1 - \tau N_{measured})\, N_{real} \tag{B.3}$$

or

$$N_{real} = \frac{N_{measured}}{(1 - \tau N_{measured})} \tag{B.4}$$

These two types of counting systems have traditionally been considered extremes of behavior such that the response of a real system would lie somewhere in between. The two curves representing the paralyzable and non-paralyzable corrections are plotted in figure 13 using $\tau = 10\ ns$. For reference, a purely linear response is also shown.

If the countrates are kept low (less than approximately 10-20 MHz in this example), the two equations give similar results. The following example illustrates the use of the non-paralyzable equation. In order to implement any count saturation correction scheme, one must determine the resolving time of the electronics. In a 100 MHz photon counting system, one would expect that the resolving time parameter would be approximately 10 ns as previously stated. The resolving time value can be determined empirically from two sets of atmospheric profiles: 1) full strength profiles 2) profiles acquired with a 10% neutral density filter in front of all PMTs. The non-paralyzable pulse pileup correction is first applied to both the full and reduced-strength signals which then allows the resolving time value to be determined for each PMT. Figure 14 shows the ratio of the count-corrected, reduced intensity profiles to the count-corrected, full-strength profiles in the high nitrogen channel for resolving times of 8, 10, 12, and 14 ns. To produce the ratios shown in the figure, the background must be subtracted from each signal. In addition, the reduced intensity and full strength profiles are normalized in order to create a value of the ratio of approximately 1.

The resolving time that yields curves that are most nearly constant with altitude is the value chosen for the later analysis. The value chosen from this figure was 11 ns in good agreement with the anticipated resolving time for 100 MHz electronics. Figure 15 results from applying the non-paralyzable pulse pileup correction to the high and low channel nitrogen data. (During CAMEX-3, the SRL used 2 PMTs per return wavelength, one for the high altitude measurement and another for the low. Both of these channels operated in the photon counting mode.) The corrected and uncorrected data are compared in this figure indicating that only the high channel data are significantly affected by the correction.

The amount of correction depends on the count rate. The count rates in the high channels are much higher than in the low channels and thus the correction is greater. In practice, for this 100 MHz system, count rates below 1 MHz are essentially uncorrected and at 10 MHz the correction amounts to about 11%. The count correction affects the high channel nitrogen data up to an altitude of approximately 4 km. Notice in the high channels that the signal is so intense in the first kilometer that the detectors are saturated and unable to provide useful photon counting data.

2.1 Non-linear photon pile-up modeling

The two traditional models of pulse pile-up described above can only produce a measured count rate that is less than the true count rate. However, real photon counting systems are actually able to display both count loss as well as count gain. Count gain can result in "super-linear" photon counting behavior; the measured number of counts can increase faster than the actual number of signal counts. A significant contribution [74] to the understanding of real photon counting systems resulted from a model of the overlapping of photon pulses that allows for both an apparent loss of counts as well as an apparent gain of counts. That mathematical model accounts for the fact that various numbers of photons that might individually not be counted may add together to exceed the threshold and thus be counted. The model developed has the form [74]

$$N = S\ exp(-\tau_d S)[P_{(a)} + P_{(1b\cap 2a)}\,(\tau_d S) + P_{(2b\cap 3a)}\frac{(\tau_d S)^2}{2} + P_{(3b\cap 4a)}\frac{(\tau_d S)^3}{3!} + \ldots] \tag{B.5}$$

where N is the measured count rate, S is the true count rate, τ_d is the system deadtime, $P_{(a)}$ is the probability that a single photon will be above the discriminator threshold, $P_{(nb\cap[n+1]a)}$ is the probability that n pulses arriving close together will be below the threshold but $n+1$ pulses arriving together will be above the threshold. One of the difficulties in implementing equation B.5 is the fact that it is double valued. Since the equation describes a counting system that is subject to paralysis, there will be two values of real count rate that can yield the observed measured count rate. In the analysis to follow, the correction was limited to the lower count rate regime to avoid this complication.

The correction using equation B.5 requires both the true count rate, S, and the measured count rate, N. These were determined by acquiring atmospheric nitrogen data both at full intensity and with a ~1% transmission neutral density filter installed. The data acquired using the neutral density filter were considered to be proportional to the true count rate since the count rate was reduced sufficiently to minimize the probability of pulse pileup. The transmission of the filter was determined by normalizing the full and 1% data at a point where the count rates were low for both of these data sets. The 1% data are then divided by the filter transmission determined by this procedure to give the "true" count rate curve, S, in equation B.5. An array of ordered pairs can then be formed of $\{N_{real}, N_{meas}\}$. This array of pairs is the data set which must be fit by the non-linear equation B.5. The general non-linear regression routine in Mathematica was used to fit this equation to the data. Using two terms in the square brackets of equation B.5, the best fit values were $\tau_d = 10.2\ ns, P_{(a)} = 0.616, P_{(1b\cap 2a)} = 0.266$. Using three terms for the equation yielded: $\tau_d = 10.8$ $ns, P_{(a)} = 0.579, P_{(1b\cap 2a)} = 0.278, P_{(2b\cap 3a)} = 0.074$. The resolving time determined using this precedure agrees well with the simpler procedure shown in figure 14.

A strict physical interpretation of these values in terms of the model would indicate that using the 2 (3) term expression for equation B.5 that the resolving time was 10.2 (10.8) ns, the probability that a count is registered by a single photon exceeding the threshold is approximately 61% (58%), while the probability that a count is registered by two closely-spaced photons that would otherwise not be counted is approximately 27% (28%). In the case of the three term equation the probability that a count is registered due to three photons adding together is about 7%. The coefficients do not add to one, which can perhaps be taken as either an indication of the uncertainty in the results or that the physics of the model used to create the equation are not exactly the physics of the counter electronics. The real value of this technique is determined by whether it extends the useful count range of the instruments and not whether the strict physical interpretation of the results is sensible.

At this point the goodness of fit of the two- and three-term forms of equation B.5 were compared to see how well they reproduced the "true" data set. The two equations were nearly indistinguishable in this respect. For simplicity, then, the two term results were used. In order to assess the performance of the non-linear correction scheme, the same set of high channel data shown in figure 15 was analyzed 1) with no correction, 2) with the non-paralyzable correction described earlier, 3) with a paralyzable correction, and 4) with the non-linear correction. The results are plotted in figure ??. The paralyzable correction is double valued in the same way as the non-linear results discussed above. As with the non-linear results, only the low count rate solution is displayed here.

In the figure, the low channel data can be taken as indicative of the shape of the linear, unsaturated profile because the actual count rate for the low channel did not exceed 1 MHz and the pulse pileup effects are much less than 1% at this count rate. For comparison purposes, therefore, the low channel data have been normalized to the high channel profiles. In increasing order of correction, or closeness to the low channel data, the processed nitrogen profiles are: raw data, non-paralyzable corrected, paralyzable corrected, and non-linear corrected. The first two of these curves are the same as shown in figure 15 but displayed on the left in terms of countrate in Hz and on the right as a ratio of the corrected results to the low channel results. The figure reveals that the raw data diverge significantly from the low channel results below an altitude of approximately 4 km. The corresponding altitudes (countrates) for the non-paralyzable, paralyzable and non-linear corrected results are approximately 2.2 km (7 MHz), 1.4 km (20 MHz), and 1.2 km (40 MHz). Therefore, the non-linear correction would allow the high channel data to be used to a lower altitude than either the non-paralyzable or paralyzable corrected data although the improvement over the paralyzable results is relatively small.

2.2 Photon pileup correction in data processing

Although the non-linear and paralyzable procedures permit photon counting data to be used at higher count rates than the non-paralyzable correction technique, the results of correcting the high-channel data using the simpler non-paralyzable approach were sufficient to permit merging of the high channel data with the low channel data at an altitude where the low channel is still providing good signal as shown in figure 15. In addition, the non-linear technique can fail to converge and, for both the non-linear and paralyzable correction techniques, the low and high solutions may not be consistent. This is taken to be due to the inherent difficulty of applying the very large correction to photon counting data that is implied through the use of the high solution in either the non-linear or paralyzable approach. Due to these considerations, the general photon counting SRL measurements during CAMEX-3 were made such that 1) the low channel count rate was low enough at every altitude to require essentially no pulse pileup correction and 2) there was a region of overlap between the low and high channels where they were both out of count saturation and could be merged reliably. In this way, the simple procedure of the non-paralyzable count correction could be used satisfactorily. The results presented in this paper were therefore obtained using the non-paralyzable correction technique.

9 References

[1] S. H. Melfi, D. N. Whiteman, R. A. Ferrare, "Observation of atmospheric fronts using Raman lidar moisture measurements", *J. App. Meteor.*, **28**, 789-806 (1989).

[2] R. A. Ferrare, Melfi S. H., Whiteman D. N., Evans K. D., "Raman Lidar Measurements of Pinatubo Aerosols over Southeastern Kansas during November - December 1991. *Geophys. Res. Lett.*, 19: (15) 1599-1602 (1992).

[3] A. J. Behrendt and J. Reichardt, "Atmospheric temperature profiling in the presence of clouds with a pure rotational Raman lidar by use of an interference-filter-based polychromator", *Appl. Opt.*, 39: (9) 1372-1378 (2000).

[4] D. D. Turner, J. E. M. Goldsmith, "Twenty-four-hour Raman lidar water vapor measurements during the Atmospheric radiation Measurement program's 1996 and 1997 water vapor intensive observation periods", *J. Atmos. Ocean. Tech.*, 16: (8) 1062-1076 (1999).

[5] D. N. Whiteman, S. H. Melfi, "Cloud liquid water, mean droplet radius and number density measurements using a Raman lidar", *J. Geophys. Res.*, **104,** No. D24, 31411-31419 (1999).

[6] A. Ansmann, U. Wandinger, M. Riebesell, C. Weitkamp, W. Michaelis, "Independent Measurement of Extinction and Backscatter Profiles in Cirrus Clouds by using a Combined Raman Elastic-Backscatter Lidar", *Appl. Opt.*, 31: (33) 7113-7131 (1992).

[7] J. Reichardt, S. Reichardt, M. Hess, T. J. McGee, "Correlations among the optical properties of cirrus-cloud particles: Microphysical interpretation", J. Geophys. Res., 107, D21, 4562 (2002).

[8] D. N. Whiteman, K. D. Evans, B. Demoz, D. O'C. Starr, D. Tobin, W. Feltz, G. J. Jedlovec, S. I. Gutman, G. K. Schwemmer, M. Cadirola, S. H. Melfi, F. J. Schmidlin, "Raman lidar measurements of water vapor and cirrus clouds during the passage of hurricane Bonnie", *J. Geophys. Res.*, 106, No. D6, 5211-5225 (2001).

[9] R. A. Ferrare, S. H. Melfi, D. N. Whiteman, K. D. Evans, R. Leifer, "Raman lidar measurements of aerosol extinction and backscattering 1. Methods and comparisons." *J. Geo. Phys. Res.*, **103**, D16, 19663-19672 (1998).

[10] B. B. Demoz, D.O'C. Starr, D.N. Whiteman, K.D. Evans, and D. Hlavka, "Raman LIDAR detection of cloud base", *Geophys. Res. Lett.*, Vol 27, No. 13, 1899-1902 (2000).

[11] D. Müller, K. Franke, F. Wagner, D. Althausen, A. Ansmann, J. Heintzenberg, "Vertical profiling of optical and physical particle properties over the tropical Indian Ocean with six-wavelength lidar 1. Seasonal cycle", *J. Geophys. Res. - Atmos.* 106: (D22) 28567-28575 (2001).

[12] D. Müller, K. Franke, F. Wagner, D. Althausen, A. Ansmann, J. Heintzenberg, G. Verver, "Vertical profiling of optical and physical particle properties over the tropical Indian Ocean with six-wavelength lidar 2. Case studies", *J. Geophys. Res. - Atmos.* 106: (D22) 28577-28595 (2001).

[13] D. N. Whiteman, G. Schwemmer, T. Berkoff, H. Plotkin, L. Ramos-Izquierdo, G. Pappalardo, "Performance modeling of an airborne Raman water vapor lidar", *Appl. Opt.*,**40**, No. 3, 375-390 (2001).

[14] S. H. Melfi,"Remote measurement of the atmosphere using Raman scattering", *Appl. Opt.*, **11**, 1605-1610 (1972).

[15] S. H. Melfi, D. Whiteman, "Observation of Lower-Atmospheric Moisture Structure and it Evolution using a Raman Lidar", *Bull. Am. Meteor. Soc.*, **66** (10) 1288-1292 (1985).

[16] G. Vaughan, D. P. Wareing, L. Thomas, V. Mitev, "Humidity measurements in the free troposphere using Raman backscatter", *Q. J. R. Meteor. Soc.*, **114**, 1471-1484 (1988).

[17] D. N. Whiteman, S.H. Melfi, and R.A. Ferrare, "Raman lidar system for the measurement of water vapor and aerosols in the earth's atmosphere", *Appl. Opt.*, **31**, No. 16, 3068-3082 (1992).

[18] A. Ansmann, M. Riebesell, C. Weitkamp, E. Voss. W. Lahmann, W. Michaelis, "Combined Raman Elastic-backscatter lidar for vertical profiling of moisture, aerosol extinction, backscatter, and lidar ratio, *Appl. Phys B.*, 55 (1), 18-28 (1992).

[19] J. E. M. Goldsmith, F. H. Blair, S. E. Bisson, D. D. Turner, "Turn-key Raman lidar for profiling atmospheric water vapor, clouds, and aerosols", *Appl. Opt.*, **37**, 4979-4990 (1998).

[20] D. D. Turner, R. A. Ferrare, L. A. H. Brasseur, W. F. Feltz, "Automated retrievals of water vapor and aerosol profiles from an operational Raman lidar", J. Atmos. Ocean. Tech., 19 (1) 37-50 (2002).

[21] J. Bösenberg, A. Ansmann, J. Baldasano, D. Balis, C. Böckmann, B. Calpini, A. Chaikovsky, P. Flamant, A. Hågård, V. Mitev, A. Papayannis, J. Pelon, D. Resendes, J. Schneider, N. Spinelli, T. Trickl, G. Vaughan, G. Visconti, M. Wiegner, "EARLINET: A European Aerosol Research Lidar Network", Proceedings of the 20th International Laser Radar Conference, Vichy (2000).

[22] J. Schneider, D. Balis, C. Böckmann, J. Bösenberg, B. Calpini, A. Chaikovsky, A. Comeron, P. Flamant, V. Freudenthaler, A. Hågård, I. Mattis, V. Mitev, A. Papayannis, G. Pappalardo, J. Pelon, M. Perrone, D. Resendes, N. Spinelli, T. Trickl, G. Vaughan, G. Visconti, "A European aerosol research lidar network to establish an aerosol climatology (EARLINET)", *J. Aerosol Sci.*, 31, Suppl. 1, 592-593 (2000).

[23] C. M. Penney, R. L. St. Peters, M. Lapp, "Absolute rotational Raman cross sections for N_2, O_2, CO_2, *J. Opt. Soc. Am.*, **64**, 5, 712-716 (1976).

[24] G. Vaughan, D. P. Wareing, S. J. Pepler, L. Thomas, V. Mitev, "Atmospheric temperature measurements made by rotational Raman scattering, *Appl. Opt.*, 32, 15, 2758-2764 (1993).

[25] Y. Arshinov and S. Bobrovnikov, "Use of a Fabry-perot interferometer to isolate pure rotational Raman spectra of diatomic molecules", *Appl. Opt.* **38**, 4635-4638 (1999).

[26] J. A. Salzman and T. A. Coney, "Remote measurement of atmospheric temperatures by Raman lidar", NASA Technical Memorandum TM X-68250 (1973).

[27] G. Herzberg, Molecular Spectra and Molecular Structure Vol. 1 - Spectra of Diatomic Molecules, Kreiger Publishing, 660 pp. (1989).

[28] D. N. Whiteman, "New examination of the traditional Raman Lidar technique II: temperature dependent aerosol scattering ratio and water vapor mixing ratio equations", *Appl. Opt.*, this issue.

[29] A. T. Young, "Revised depolarization corrections for atmospheric extinction", *Appl. Opt.*, 19: (20) 3427-3428 (1980).

[30] A. T. Young, "On the Rayleigh-Scattering Optical Depth of the Atmosphere", *J. Appl. Meteor.*, 20, 328-330

(1980).

[31] Lord Rayleigh, "On the light from the sky, its polarization and color", *Phil. Mag.*, **41**, 107-120,274-279 (1871).

[32] Lord Rayleigh, "On the scattering of light by small particles", *Phil. Mag.*, **41**, 447-454 (1871).

[33] M. Born. and E. Wolf, *Principles of Optics*, Cambridge University Press, 952 pp. (1999).

[34] R. M. Measures, *Laser Remote Sensing Fundamentals and Applications,* (Wiley-Interscience, New York, New York, 1984).

[35] V. Sherlock, A. Hauchecorne, J. Lenoble, "Methodology for the independent calibration of Raman backscatter water-vapor lidar systems", *App. Opt.*, **38**, 27, 5816-5837 (1999).

[36] G. Avila, J. M. Fernandez, B. Mate, G. Tejeda, S. Montero, "Ro-vibrational Raman Cross Sections of Water Vapor in the OH Stretching Region", *J. Mol. Spectr.*, **196**, 77-92 (1999).

[37] D. N. Whiteman,W. F. Murphy, N. W. Walsh, K. D. Evans, "Temperature sensitivity of an atmospheric Raman lidar system based on a XeF excimer laser", *Opt. Lett.*, **18**, No. 3, 247 - 249 (1993).

[38] D. N. Whiteman, G. E. Walrafen, W.-H. Yang, S. H. Melfi, "Measurement of an isosbestic point in the Raman spectrum of liquid water using a backscattering geometry", Appl. Opt., 38, 2614-2615 (1999).

[39] M. Mitev, I. V. Grigorov, V. B. Simeonov, "Lidar measurement of atmospheric aerosol extinction profiles - a comparison between 2 techniques - Klett inversion and pure rotational Raman-scattering methods", *Appl. Opt.*, 31 (30) 6469-6474 (1992).

[40] W. S. Heaps, J. Burris, J. A. French, "Lidar technique for remote measurement of temperature by use of vibrational-rotational Raman spectroscopy", *Appl. Opt.* 36: (36) 9402-9405 (1997).

[41] W. F. Murphy, "Ro-vibrational Raman-spectrum of water-vapor nu-2 and 2-nu-(2)", *Mol. Phys.* 33: (6) 1701-1714 (1977).

[42] W. F. Murphy W. F., "Ro-vibrational Raman-spectrum of water-vapor nu-1 and nu-3", *Mol. Phys.* 36: (3) 727-732 (1978).

[43] J. M. Fernendez-Sanchez and W. F. Murphy, "Raman-scattering cross sections and polarizability derivatives for H_2S, D_2S and HDS", *J. Mol. Spectrosc.* 156: (2) 431-443 (1992).

[44] J. M. Fernendez-Sanchez and W. F. Murphy, "True and effective polarizability tensors for asymmetric-top molecules - the rotational Raman-spectra of H2S and D2S", *J. Mol. Spectrosc.* 156: (2) 444-460 (1992).

[45] J. M. Fernandez, Instituta Estructura Matera, Madrid, Spain (personal communication, 1999).

[46] D. A. Long, Raman Spectroscopy, McGraw-Hill, New York, 1977.

[47] C-Y. She, "Spectral structure of laser light scattering revisited: bandwidths of nonresonant scattering lidars", *Appl. Opt.*, 40, 27, 4875-4884 (2001).

[48] P. A. T. Haris, "Pure Rotational Raman Lidar for Temperature Measurements in the Lower troposphere", Ph.D. Dissertation Pennsylvania State University (1995).

[49] M. Bass,(Ed.), "Handbook of Optics", McGraw-Hill, Inc., in 2 volumes. (1995).

[50] U. S. Standard Atmosphere, 1976. NOAA document S/T 76-1562, National Oceanic and Atmospheric Administration, National Aeronautics and Space Administration, United States Air Force, Washington, DC 227 pp.

[51] A. M. Bass and R. J. Paur, "Ultraviolet cross-sections of ozone, I. Measurements" in Atmospheric Ozone, Proc. Quadrennial Ozone Symposium, C. S. Zerophos and A. Ghanzi, eds., D. Reidel, Hingham, Mass (1985).

[52] Modtran 4 Radiative Transfer Code, The Air Force Research Lab, Space Vehicles Directorate. Hanscom Air Force Base, MA

[53] D. R. Bates, "Rayleigh Scattering By Air", *Planet. Space Sci.*, 32, 6, 785-790 (1984).

[54] A. Bucholtz, "Rayleigh-scattering calculations for the terrestrial atmosphere". *Appl. Opt.*, 34, 15, 2765-2773 (1995).

[55] E. R. Peck and K. Reeder, "Dispersion of air". *J. Opt. Soc. Am.*, **62**, 958-962 (1972).

[56] R. M. Goody and Y. L. Yung, "Atmospheric Radiation Theoretical Basis", Oxford University Press, Oxford, England. pp. 519 (1989).

[57] S. Chandrasekhar, "Radiative Transfer", Dover Publications, Inc., New York, New York, pp. 393, (1960).

[58] A. Ansmann, M. Riebesell, and C. Weitkamp, "Measurement of atmospheric aerosol extinction profiles with a Raman lidar," *Optics Letters*, **15**, 13, 746-748 (1990).

[59] R. T. H. Collis and P. B. Russell, "Lidar Measurement of Particles and Gases by Elastic Backscattering and Differential Absorption", in *Laser Monitoring of the Atmosphere*, (E. D. Hinkley, Ed., Spinger-Verlag, 1976).

[60] D. N. Whiteman, "Application of Statistical Methods to the Determination of Slope in Lidar Data", Appl. Opt., 38, 15, 3360-3369 (1999).

[61] E. P. Shettle and R. W. Fenn, "Models for the Aerosols of the Lower Atmosphere and the Effects of Humidity Variations on Their Optical Properties", Air Force Geophysics Laboratory document AFGL-TR-79-0214 (1979).

[62] E. P. Hamonou, P. Chazette,D. Balis, F. Dulac, X. Schneider, E. Galani, G. Ancellet, A. Papayannis, "Characterization of the vertical structure of Saharan dust export to the Mediterranean basin", *J. Geophys. Res. - Atmos.*, 104: (D18) 22257-22270 (1999).

[63] S. Kato, M. H. Bergin, T. P. Ackerman, T. P. Charlock, E. E. Clothiaux, R. A. Ferrare, R. N. Halthore, N. Laulainen, G. G. Mace, J. Michalsky, D. D. Turner, "A comparison of the aerosol thickness derived from ground-based and airborne measurements", *J. Geophys. Res. - Atmos.*, 105: (D11) 14701-14717 (2000).

[64] T. Eck, Aeronet group - NASA/Goddard Space Flight Center, (personal communication, 2002).

[65] P. R. Bevington and D. K. Robinson, *Data Reduction and Error Analysis for the Physical Sciences*, McGraw-Hill, 328 pp (1992).

[66] U. Wandinger, "Multiple-scattering influence on extinction- and backscatter-coefficient measurements with Raman and high-spectral-resolution lidars", *Appl. Opt.*, **37**, 3, 417-427 (1998).

[67] E. W. Eloranta, E. W., "Practical model for the calculation of multiply scattered lidar returns", *Appl. Opt.*, **37**,12, 2464-2472 (1998).

[68] T. N. Carlson, and Prospero, J.M., 1972; The large-scale movement of Saharan air outbreakes over the northern equatorial Atlantic. J. Appl. Meteor., 11, 283-297.

[69] J. M. Prospero,R.A. Glaccum, and R.T. Nees, 1981; Atmospheric transport of soil dust from Africa to South America, Nature, 289, 570-572.

[70] L. Schutz, R. Jaenicke, and H. Pietrek, 1981; Saharan dust transport over the North Atlantic Ocean, Geological Society of America Special Paper 186, 87-100.

[71] A. di Sarra, T. Di Iorio, M. Cacciani, G. Fiocco, D. Fuà, "Saharan dust profiles measured by lidar at Lampedusa", *J. Geophys. Res.*, 106 D10, 10335-10347 (2001).

[72] O. Dubovik, B. Holben, T. Eck, A. Smirnnov, Y. Kaufman, M. King, D. Tanre, I. Slutsker, "Variability of Absorption and Optical Properties of Key Aerosol Types Observed in Worldwide Locations, *J. Atmos. Sci.*, 59, 590-608.

[73] R. D. Evans, *The Atomic Nucleus*, (McGraw-Hill, New York 1955).

[74] D. P. Donovan, J. A. Whiteway, A. I. Carswell, "Correction for nonlinear photon-counting effects in lidar systems", *App. Opt.* **32**, 33, 6742-6753 (1993).

10 Figure Captions

1. Raman scattering spectrum for the OH-stretch region of the spectrum simulated using a 0.5 cm^{-1} slit width and at two temperatures: 200 K and 295 K. Also shown is a representation of a ~18 cm^{-1} (0.3 nm when excited at 354.7 nm) passband centered at 3654 cm^{-1} that could be used for the detection of the water vapor signal. The y-axis is in arbitrary units.
2. The integral of the Raman differential backscatter cross section and transmission of the passband shown in figure 1. The transmitted intensity at 200K is approximately 7% larger than at 300K.
3. Ratio of transmitted intensities at 200K and 300K for Rayleigh and Raman (water vapor, nitrogen and oxygen) passbands for widths up to 300 cm^{-1} (~5 nm for excitation at 354.7 nm).
4. The ratio of transmitted intensities for water vapor passbands of varying widths and center position where the center positions, shown in the legend, are given in units of wavenumbers (cm^{-1}). For reference, a filter width of 60 cm^{-1}corresponds to ~1 nm for excitation at 354.7. The corresponding wavelengths (nm) of the filter center positions when excited at 354.7 nm and 532.07 can be found in table 2
5. The temperature dependent functions $F_R(r)$, $F_O(r)$, $F_N(r)$, $F_H(r)$ that are needed to evaluate the Rayleigh-Mie and Raman lidar equations are plotted as a function of altitude assuming the U. S. Standard Atmosphere temperature profile. The bandwidths (noted in cm^{-1} in the legend) correspond to 0.3 nm and 2.0 nm when excited by 354.7 nm radiation.
6. Comparison of 3 formulations of total Rayleigh scattering cross section: 1) the full treatment shown in equation 12 and indicated by $\rho = \rho(\lambda)$ in the legend, 2) the same equation but with a constant depolarization value of 0.0279 [30], and 3) the same equation but neglecting the King factor. Significant differences are produced by use of either of the approximate methods.
7. The ratio of two formulations of the Rayleigh backscatter coefficient, given by equations 21 and 19, is plotted from 250 to 1000 nm. The difference between the simple numerical formula and equation 19 increases to more than 10% at short wavelengths.
8. Aerosol extinction (at 351 nm) calculated from a 20 minute average of data from the night of August 26, 1998 at Andros Island, Bahamas. The sensitivity of the aerosol scaling parameter, k, is tested here.
9. Six synthetic aerosol extinction profiles created to test the influence of multiple scattering on measurements of aerosol extinction. Three are for use in the simulations of elevated dust layers while the other three are for simulation of boundary layer aerosols. The desert dust profiles are referred to as DD(τ) where τ is the optical depth of the layer. The corresponding key for the boundary layer aerosols is BL.
10. Multiple scattering simulations for the boundary layer aerosol profiles shown in figure 9. Calculations assuming

constant size aerosols of 0.5 micron radius are shown on the left and 2.0 microns on the right. The error in extinction is plotted for the high optical depth case on the right.

11. Multiple scattering simulations for a layer of desert dust between 5 and 6 km. The mean particle size used is 3 microns and three optical depths are studied 0.1, 0.25, and 0.5. The error in extinction is also plotted for the 0.5 optical depth case.

12. Probability of measuring n counts for a Poisson process characterized by a mean countrate of 40 counts per unit time.

13. Comparison of paralyzable and non-paralyzable count corrections using a resolving time of 10 $nsec$. The observed count rate of a paralyzable system tends toward zero with increasing true count rate. The observed count rate of a non-paralyzable system tends toward the maximum countrate as the real count rate increases. A perfect linear system is also represented.

14. Comparison of photon pulse pileup corrections for a range of resolving time values using a non-paralyzable count correction procedure. The resolving time yielding the curve closest to a constant with altitude is chosen for the later processing. For the high nitrogen channel shown here, the choice of a resolving time of 11 $nsec$ yields a pulse pileup correction that agrees with the low intensity signal to within ~1% for altitudes above ~3 km.

15. Low (left) and high (right) channel nitrogen data are shown with and without the non-paralyzable count correction using a value of 11 $nsec$ for the deadtime. The correction is only apparent above approximately 1 MHz so that the correction has much more effect on the high channel data.

16. Comparison of different methods of correcting for effects due to photon pulse pileup. The same nitrogen data treated in figure 15 are again analyzed here. The raw data (NoCorr) are shown along with non-paralyzable, paralyzable and non-linear corrections (NPCorr, ParCorr, NLCorr). The low channel data (Lo), normalized to the high count rate (Hz), are also shown as an indication of the true count rate.

11 Table Captions

1. Calculations of the F_x factor for various lidar passband widths (FWHM) corresponding to 0.3 nm ("narrow") and 2.0 nm ("wide") when excited at 354.7 nm. The water vapor transmission width corresponds to 0.3 nm excited at the same wavelength. The percentage change in the effective cross section between 200K and 300K is shown for each case as an indication of the temperature sensitivity for tropospheric measurements. Changes in the Rayleigh function F_R for a 24 cm^-1 wide passbandare after the third decimal place.
2. Table for converting between passbands expressed in wavenumbers and wavelength at either 354.7 nm or 532.07 nm.
3. Conversion table for center position of water vapor passbands.

12 Tables

13 Figures

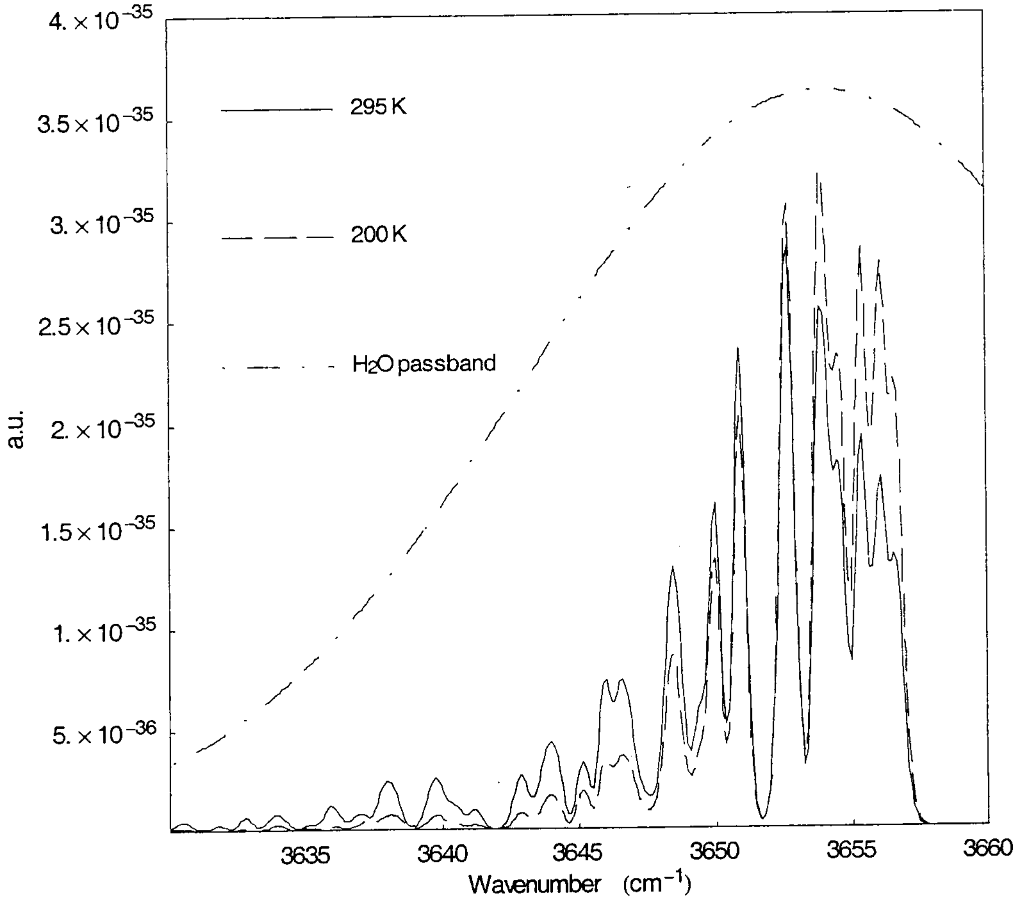
4. × 10^-35
3.5 × 10^-35
3. × 10^-35
2.5 × 10^-35
2. × 10^-35
1.5 × 10^-35
1. × 10^-35
5. × 10^-36
a.u.
295 K
200 K
H2O passband
3635
3640
3645
3650
3655
3660
Wavenumber (cm^-1)

Figure 1:

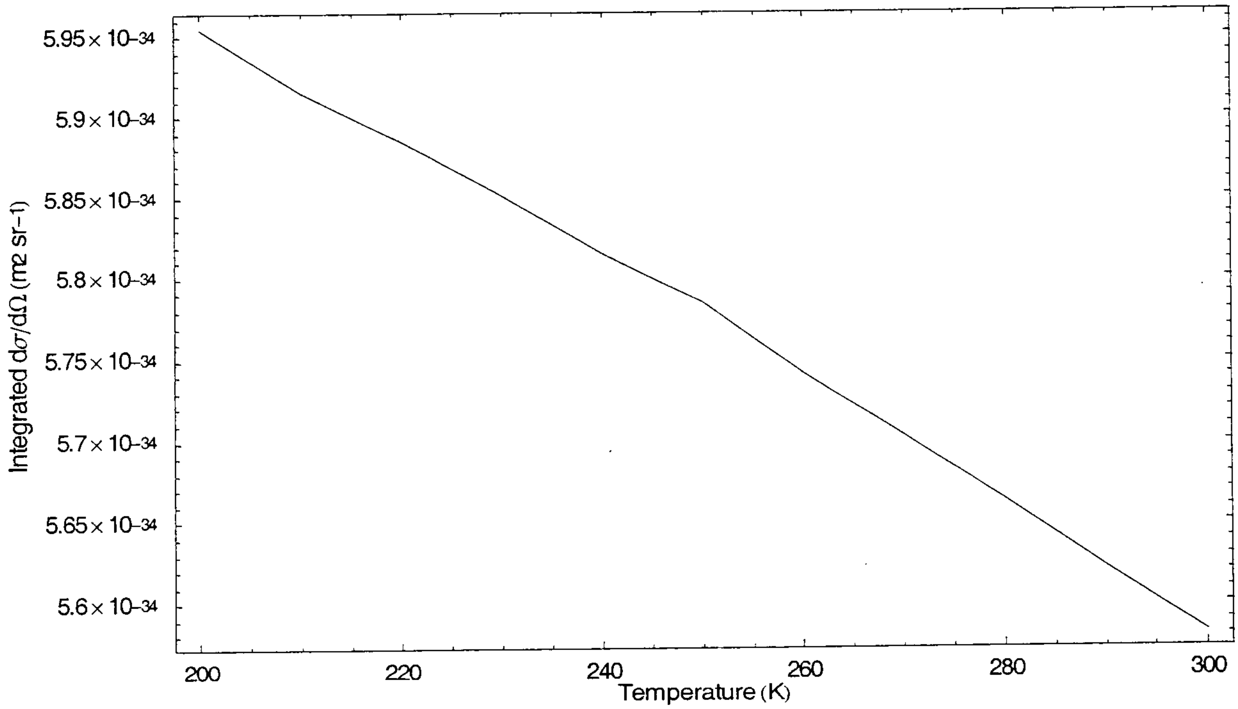
5.95 × 10-34
5.9 × 10-34
5.85 × 10-34
5.8 × 10-34
5.75 × 10-34
5.7 × 10-34
5.65 × 10-34
5.6 × 10-34
Integrated dσ/dΩ (m2 sr-1)
200
220
240
260
280
300
Temperature (K)

Figure 2:

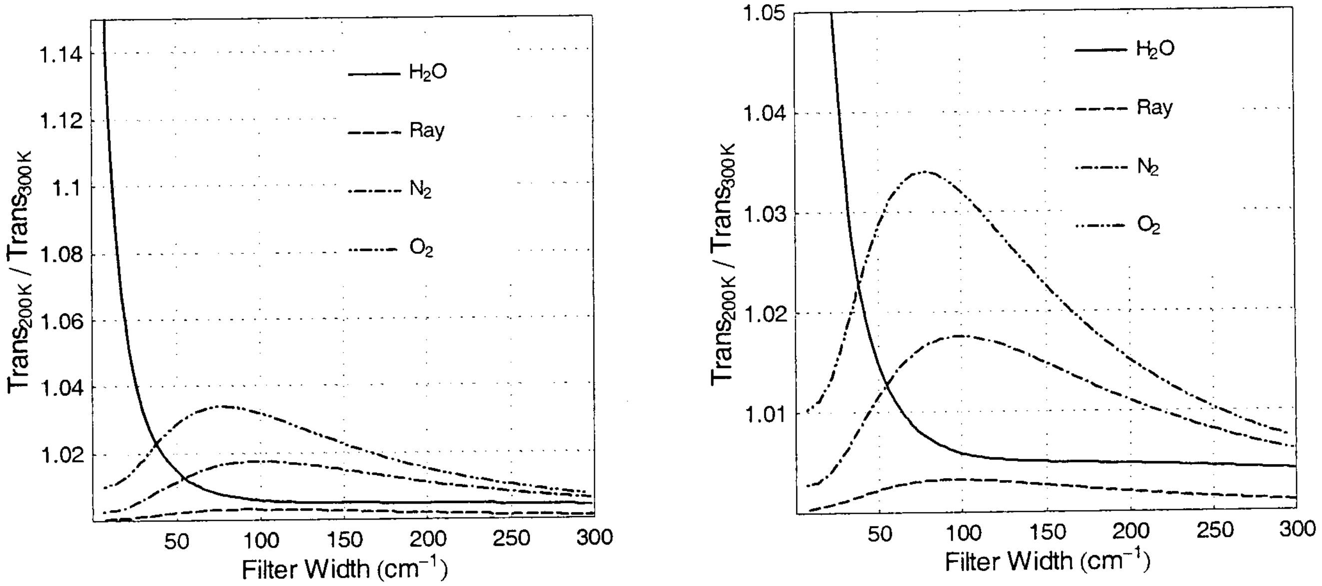

Figure 3:

F_X for selected passband center and width combinations

		Effective cross section as f(T)						Percent Change ($I_{200K}/I_{300K} \times 100$)
	Passband ($\nu_0(cm^{-1}), \Delta\nu(cm^{-1})$)	200K	220K	240K	260K	280K	300K	
Narrow	Rayleigh $(0, 24)$	0.970	0.970	0.970	0.970	0.970	0.970	0.1
	Oxygen $(1556, 21)$	0.749	0.746	0.744	0.742	0.741	0.734	1.33
	Nitrogen $(2331, 20)$	0.851	0.850	0.8493	0.850	0.848	0.848	0.39
	Water vapor $(3654, 18)$	0.961	0.950	0.938	0.926	0.913	0.900	6.7
Wide	Water vapor $(3654, 120)$	0.997	0.995	0.993	0.992	0.990	0.988	0.9
	Rayleigh $(0, 159)$	0.992	0.992	0.991	0.991	0.990	0.990	0.26
	Oxygen $(1556, 142)$	0.933	0.929	0.924	0.920	0.915	0.911	2.42
	Nitrogen $(2331, 134)$	0.947	0.944	0.940	0.938	0.9345	0.931	1.61
	Water vapor $(3654, 120)$	0.997	0.995	0.993	0.992	0.990	0.988	0.9

Passband width conversion table

	Excitation wavelength (nm)	354.7				532.07			
	Molecule (Δcm^{-1})	"Air" (0)	O_2 (1556)	N_2 (2331)	H_2O (3654)	"Air" (0)	O_2 (1556)	N_2 (2331)	H
	Shifted wavelength (nm)	354.7	375.4	386.7	407.5	532.07	580.1	607.4	6
Width (cm^{-1})		Width (nm)							
25		0.31	0.35	0.37	0.42	0.71	0.84	0.92	1.
50		0.63	0.70	0.75	0.83	1.42	1.68	1.85	2.
100		1.26	1.41	1.50	1.66	2.83	3.37	3.69	4.
150		1.89	2.13	2.24	2.49	4.25	5.05	5.54	6.
200		2.52	2.82	2.99	3.32	5.67	6.74	7.39	8.
250		3.15	3.52	3.74	4.15	7.09	8.42	9.24	1
300		3.77	4.23	4.49	4.98	8.50	10.1	11.08	1

Table 2: Table for converting between passbands expressed in wavenumbers and wavelength at either 354.7 nm or 532.07 nm

Passband center conversion table

	Excitation wavelength (nm)	
	354.71	532.07
Shift (cm^{-1})	Wavelength (nm)	
3649	407.45	660.25
3650	407.46	660.30
3651	407.48	660.34
3652	407.50	660.38
3653	407.51	660.43
3654	407.53	660.47
3655	407.55	660.52
3656	407.56	660.56

Table 3: Conversion table for center position of water vapor passbands.

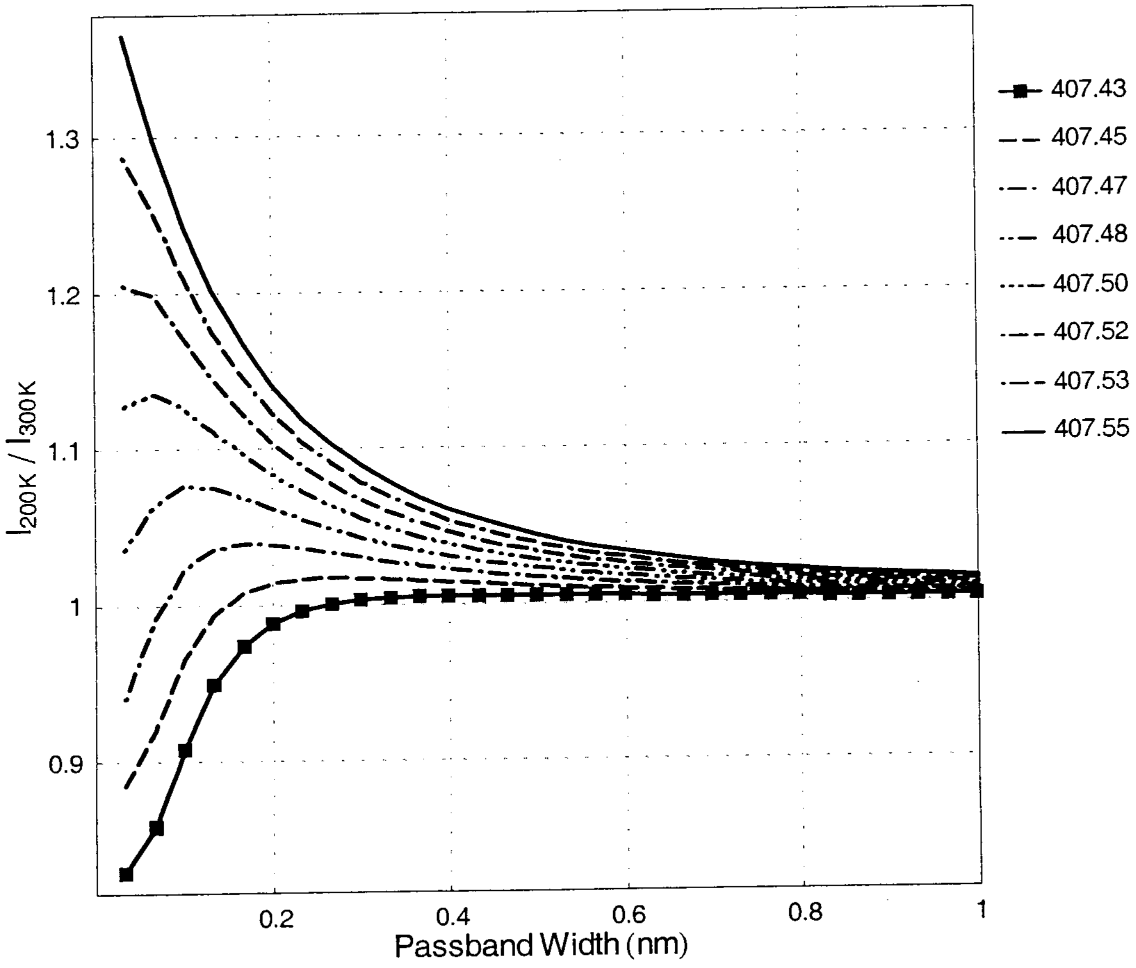
1.3
1.2
1.1
1
0.9
I_{200K} / I_{300K}
0.2
0.4
0.6
0.8
1
Passband Width (nm)
407.43
407.45
407.47
407.48
407.50
407.52
407.53
407.55

Figure 4:

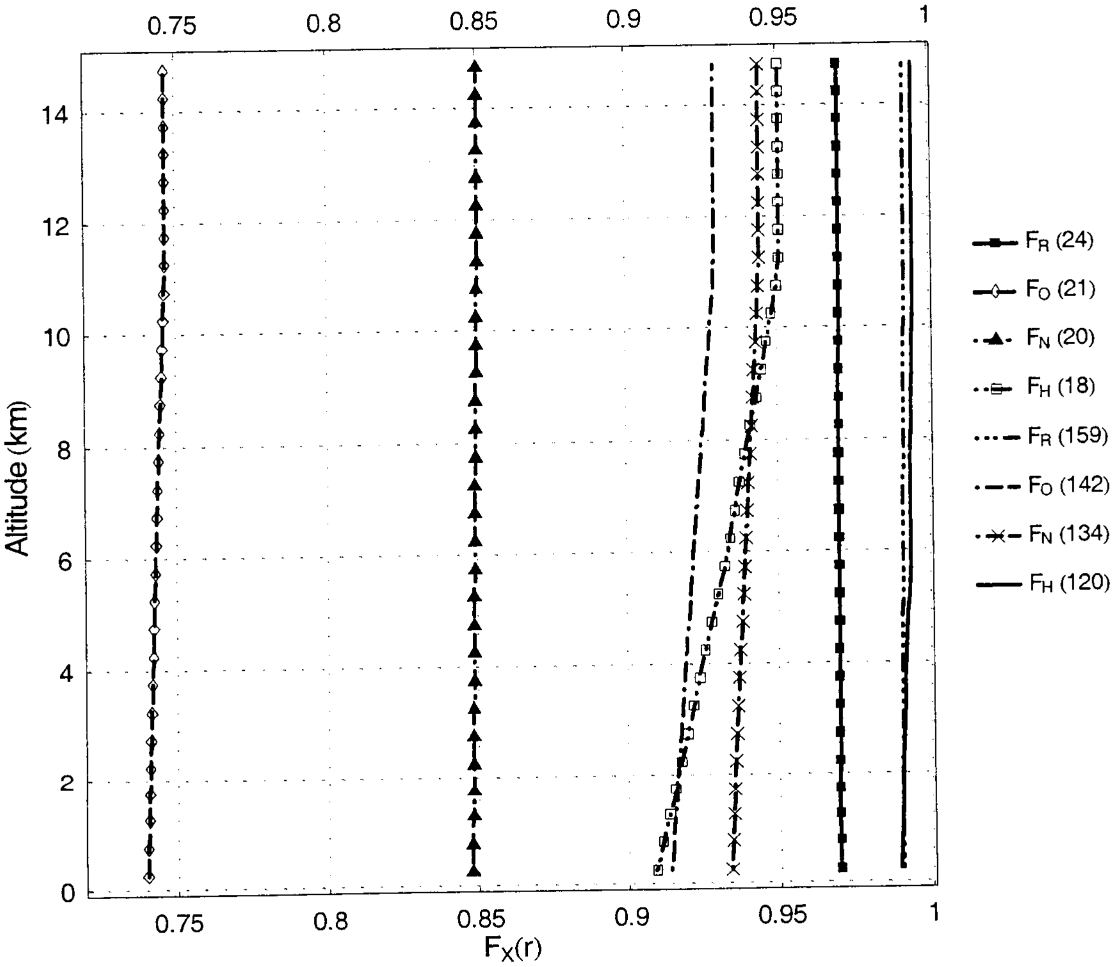
0.75
0.8
0.85
0.9
0.95
1
14
12
10
8
6
4
2
0
Altitude (km)
0.75
0.8
0.85
0.9
0.95
1
$F_X(r)$
F_R (24)
F_O (21)
F_N (20)
F_H (18)
F_R (159)
F_O (142)
F_N (134)
F_H (120)

Figure 5:

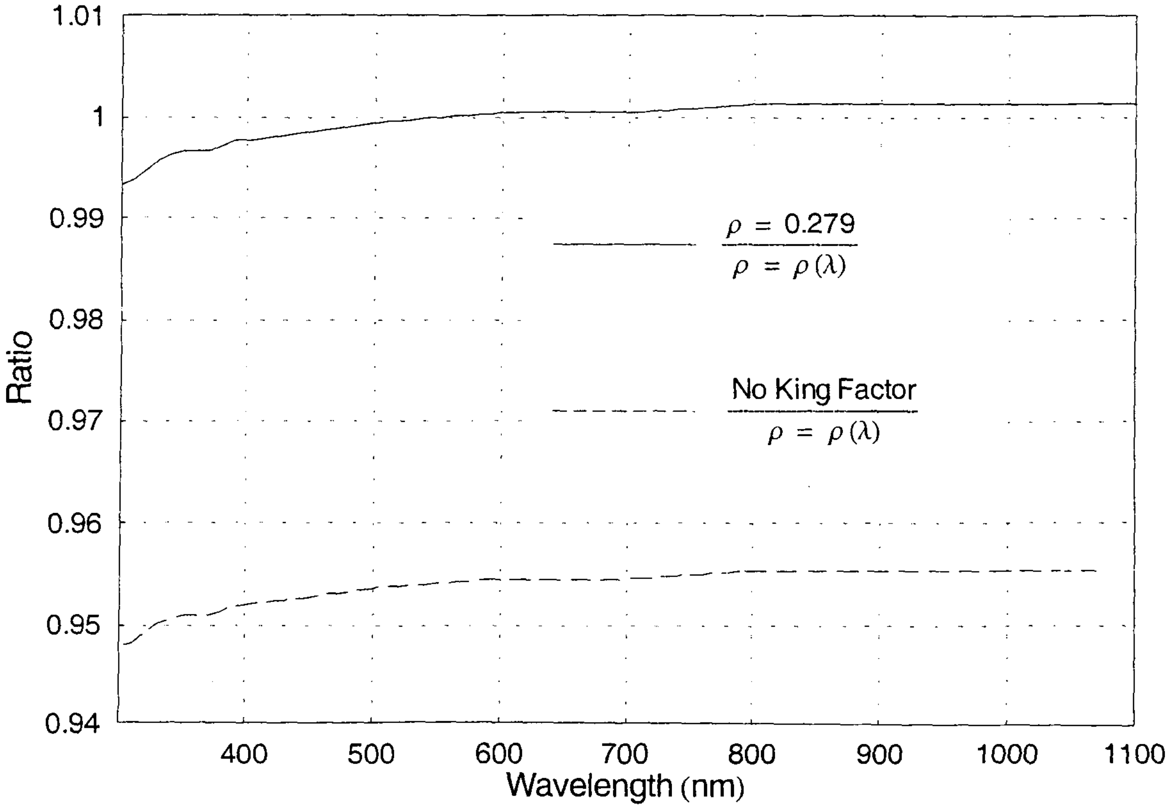
1.01
1
0.99
0.98
0.97
0.96
0.95
0.94
Ratio
400
500
600
700
800
900
1000
1100
Wavelength (nm)
$\frac{\rho = 0.279}{\rho = \rho(\lambda)}$
$\frac{\text{No King Factor}}{\rho = \rho(\lambda)}$

Figure 6:

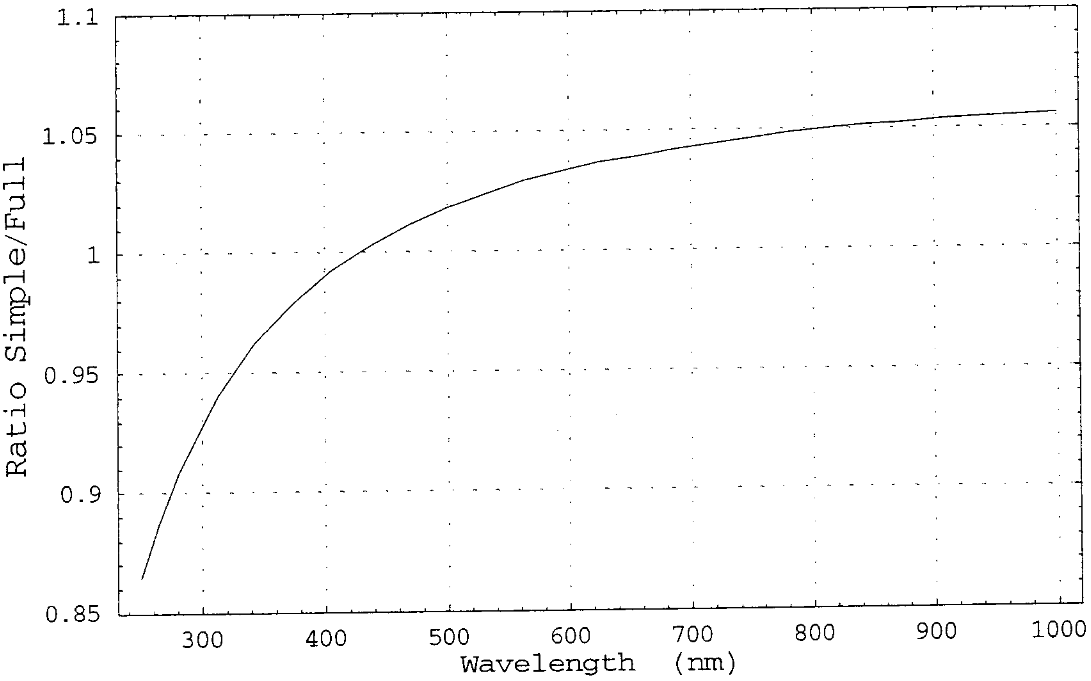
1.1
1.05
1
0.95
0.9
0.85
Ratio Simple/Full
300
400
500
600
700
800
900
1000
Wavelength (nm)

Figure 7:

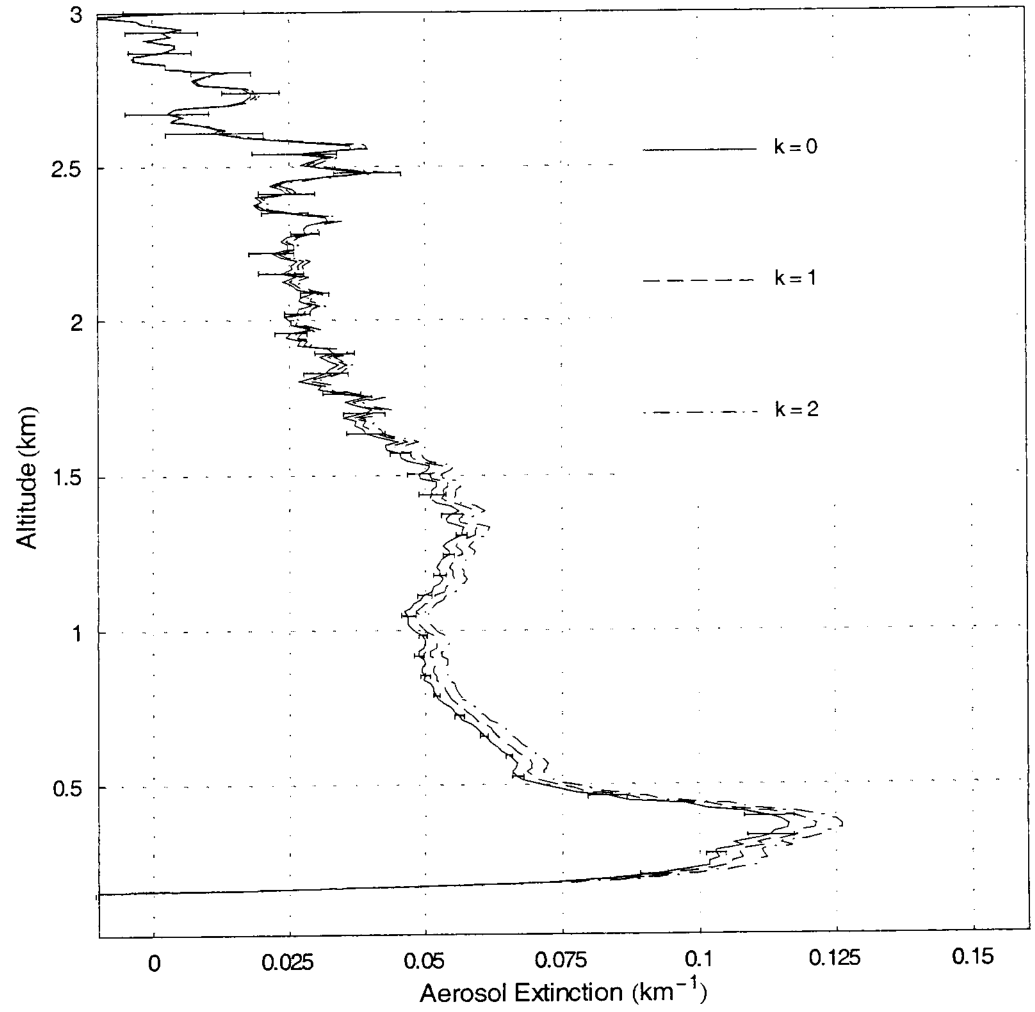
3
2.5
2
1.5
1
0.5
Altitude (km)
0
0.025
0.05
0.075
0.1
0.125
0.15
Aerosol Extinction (km^{-1})
k = 0
k = 1
k = 2

Figure 8:

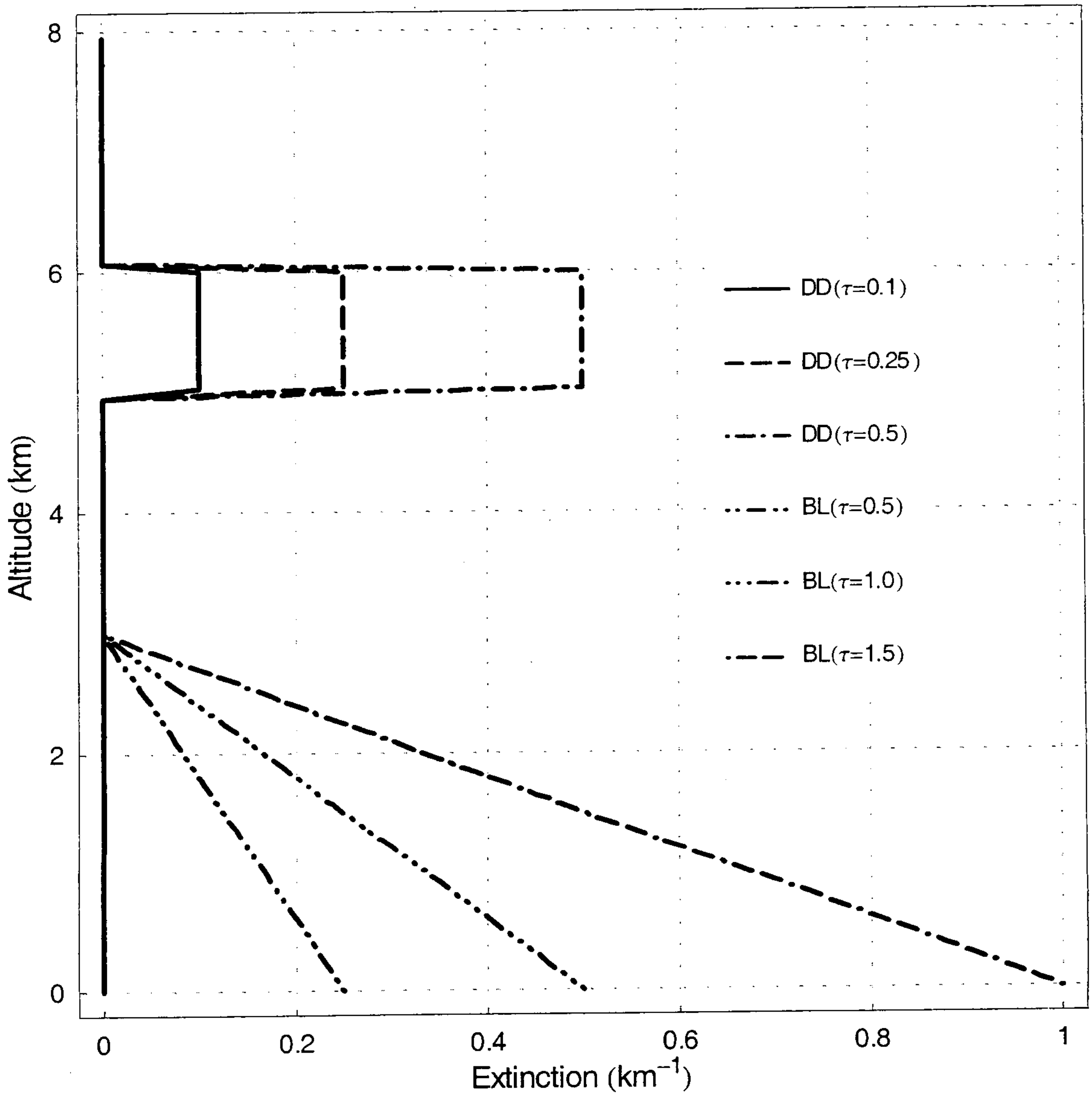
8
6
4
2
0
Altitude (km)
0
0.2
0.4
0.6
0.8
1
Extinction (km^{-1})
DD(τ=0.1)
DD(τ=0.25)
DD(τ=0.5)
BL(τ=0.5)
BL(τ=1.0)
BL(τ=1.5)

Figure 9:

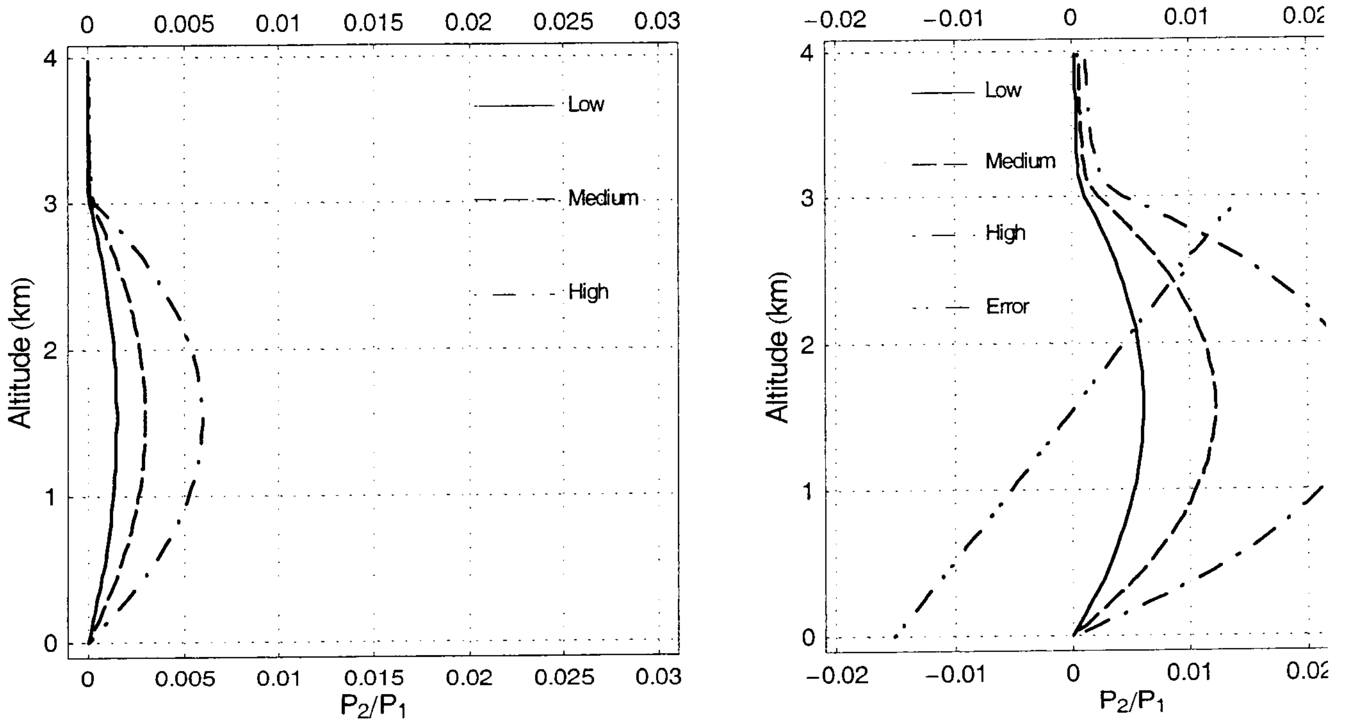
0
0.005
0.01
0.015
0.02
0.025
0.03
Altitude (km)
4
3
2
1
0
Low
Medium
High
P2/P1
−0.02
−0.01
0
0.01
0.02
Low
Medium
High
Error

Figure 10:

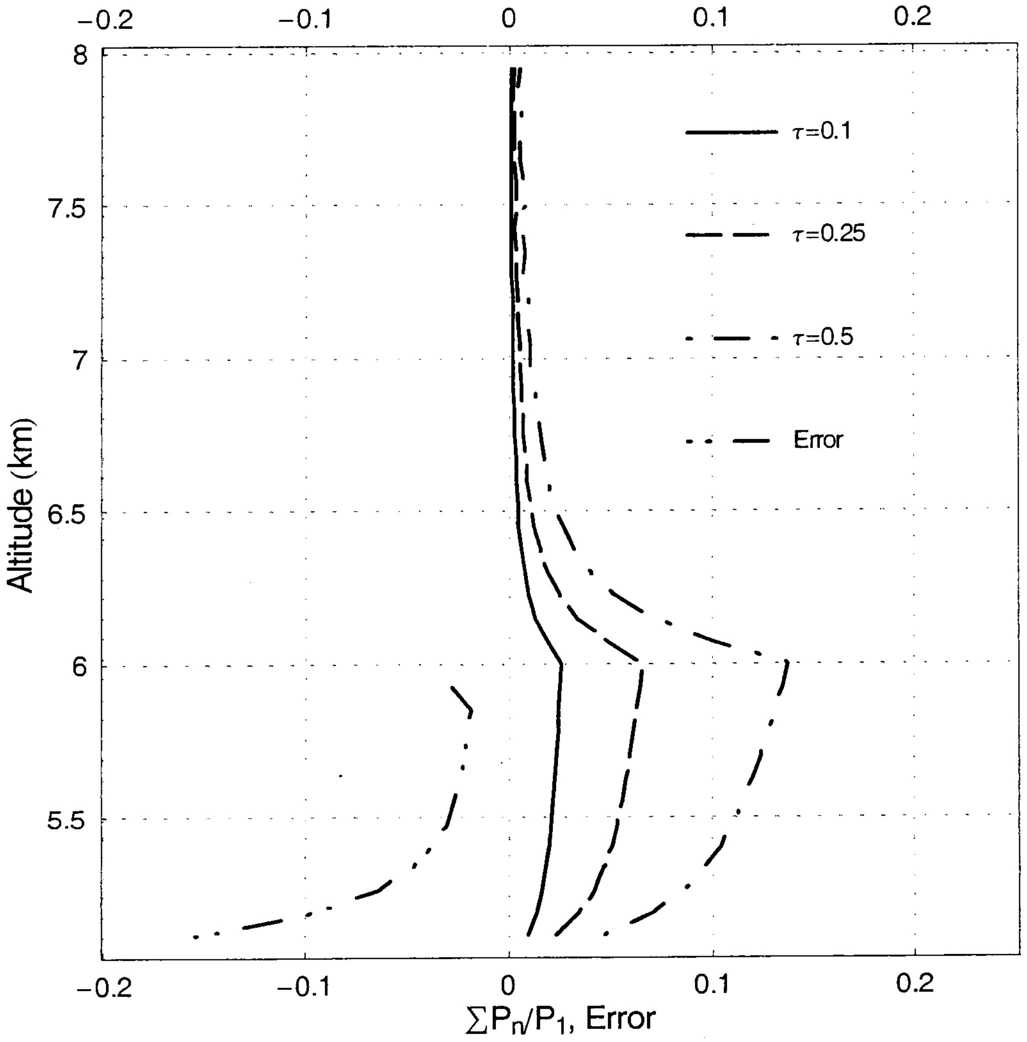

−0.2
−0.1
0
0.1
0.2
8
7.5
7
6.5
6
5.5
Altitude (km)
τ=0.1
τ=0.25
τ=0.5
Error
−0.2
−0.1
0
0.1
0.2
∑Pn/P1, Error

Figure 11:

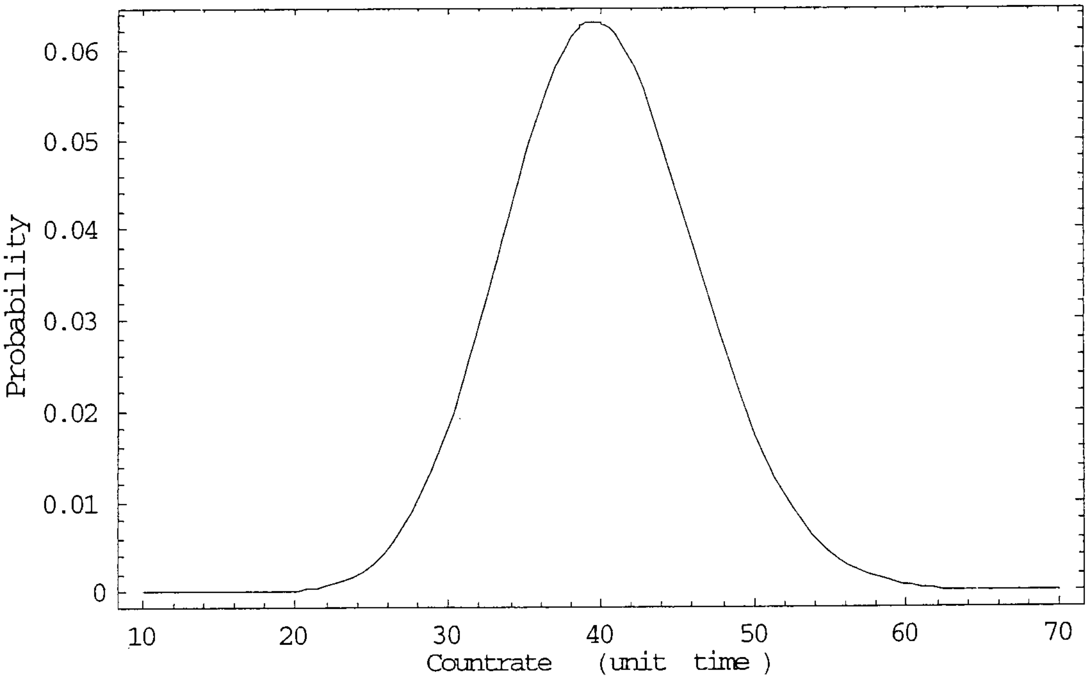

0.06
0.05
0.04
0.03
0.02
0.01
0
Probability
10
20
30
40
50
60
70
Countrate (unit time)

Figure 12:

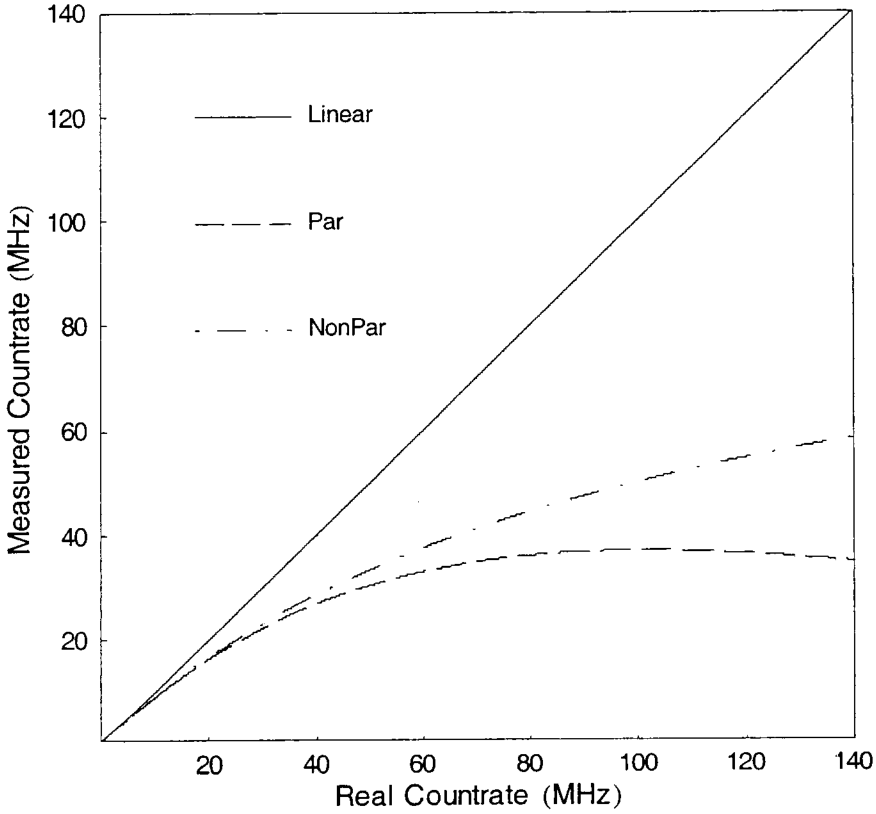
Linear
Par
NonPar
Measured Countrate (MHz)
Real Countrate (MHz)
20
40
60
80
100
120
140

Figure 13:

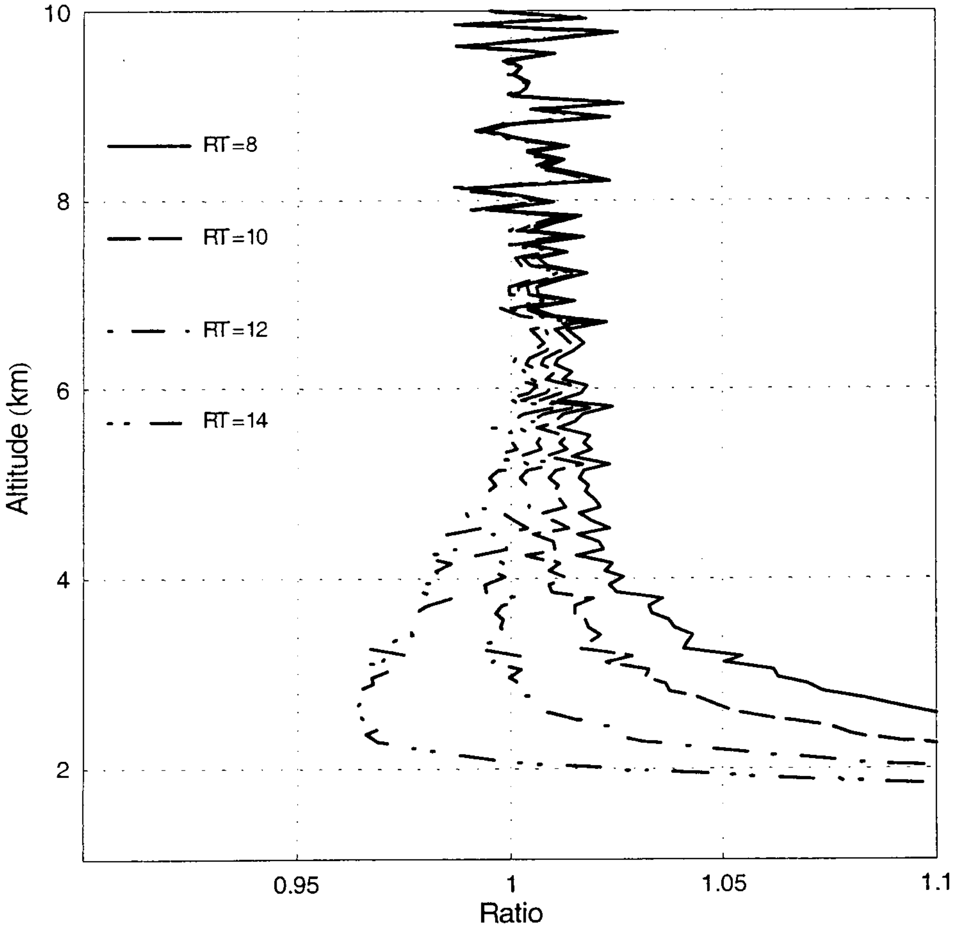

Figure 14:

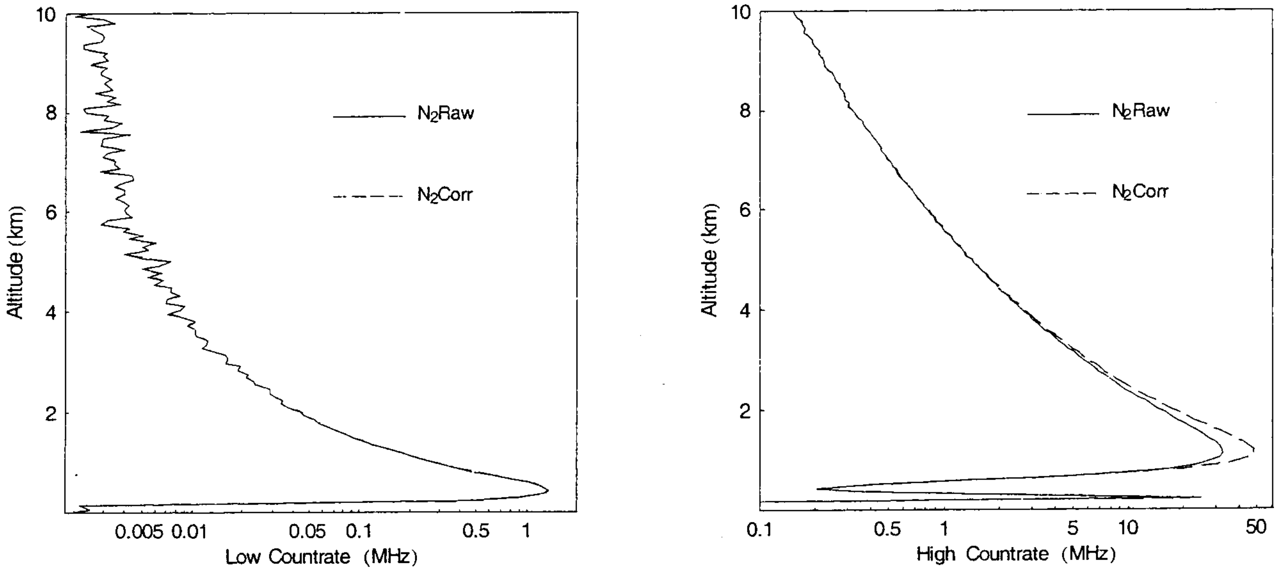
Altitude (km)
10
8
6
4
2
0.005 0.01
0.05 0.1
0.5 1
Low Countrate (MHz)
N_2Raw
N_2Corr
Altitude (km)
10
8
6
4
2
0.1
0.5 1
5 10
50
High Countrate (MHz)
N_2Raw
N_2Corr

Figure 15: